8-27-2009

The development of nanofluidic platforms for biomolecular separations

Anthony Garcia

Anthony L. Garcia.

Candidate

Mechanical Engineering

Department

This dissertation is approved, and it is acceptable in quality and form for publication:

Approved by the Dissertation Committee:

ANDREA MANNOLI, Chairperson

DIMITER PETSEV

C. Randall Truman

Gabriel Lopez

The Development of Nanofluidic Platforms for Biomolecular Separations

by

Anthony L. Garcia

B.S., Mechanical Engineering, Univ. of New Mexico, 2002

M.S., Mechanical Engineering, Univ. of New Mexico 2008

DISSERTATION

Submitted in Partial Fulfillment of the

Requirements for the Degree of:

Doctor of Philosophy in

Engineering

The University of New Mexico

Albuquerque, New Mexico

August 2009

Dedication

For the giants upon whose shoulders I've been standing on…

Acknowledgments

Thanks to my family, friends, and colleagues who were an inspiration through it all; especially to my grandfather, who always wanted me to get as much education as possible.

Thanks to my advisors Professor Gabriel P. Lopez and Professor Andrea A. Mammoli who always pushed me to do better. Thanks to the other members of my dissertation committee: Professor Dimiter N. Petsev, and Professor C. Randall Truman

Thanks to all my friends at the University of New Mexico, especially Brett Andrzejewski and Tomas Gamble, who were there from the start.

Thanks to the IGERT/CORE program and all of the fellows, staff, and faculty involved at the University of New Mexico.

Thanks to Heather Williams who always kept graduation possible.

The work presented in this dissertation was done in collaboration with many brilliant people. The experimental procedures were developed with the help of Linnea Ista, Dr. Michael O'Brien, and Nichlaus Carroll. The fabrication was carried out with Dr. Michael O'Brien, Tomas Gamble, Alexander Neumann, and Paul Bisong. The theoretical work was developed in conjunction with Dr. Dimiter Petsev. Additional technical advisement was provided by Dr. Sang Han, Dr. Younjin Oh, Dr. Scott Sibbett, and Dr. Steven R.J. Brueck. The computer program used for extrapolating velocity data from experiments was written by Dr. Kateryna Artyushkova.

This work was funded by the NSF-IGERT Fellowship, the NSF-PREM Fellowship, and the W.M. Keck Foundation.

The Development of Nanofluidic Platforms for Biomolecular Separations

by

Anthony L. Garcia

B.S., Mechanical Engineering, Univ. of New Mexico, 2002

M.S., Mechanical Engineering, Univ. of New Mexico 2008

ABSTRACT OF DISSERTATION

Submitted in Partial Fulfillment of the

Requirements for the Degree of

Doctor of Philosophy in

Engineering

The University of New Mexico

Albuquerque, New Mexico

August 2009

The Development of Nanofluidic Platforms for Biomolecular Separations

by

Anthony L. Garcia

B.S., Mechanical Engineering, Univ. of New Mexico, 2002

M.S., Mechanical Engineering, Univ. of New Mexico 2008

PhD., Mechanical Engineering, Univ. of New Mexico 2009

Abstract

Recently the extrication and purification of important biomolecules, especially proteins, has been a topic of great interest. Common systems used in the purification and extraction of these important biological molecules includes gel electrophoresis, various forms of chromatography, and capillary electrophoresis type devices. These systems, while achieving a good amount of success, each possess inherent properties that can be improved upon. They usually necessitate comparatively large laboratory footprints, require high voltages to operate (in the tens of kilovolts), and call for relatively large

sample sizes in order to perform these tasks. All of these shortcomings can be addressed by performing these separations and purifications in smaller, nanofluidic based systems.

This dissertation presents research conducted to explore how fluids, electrical fields, and dissolved analytes of interest (including biomolecules) behave in nanoconfined systems. It presents the recent advances in fabrication that allow for such studies to be embarked upon. It also presents various experimental methodologies for performing investigational work within nanofluidic systems. These include the development of observation techniques, the various methods of controlling nanofluidic transport, buffers, surfactants, and analyte selection. Several techniques for performing separations that are unique to nanofluidic systems are explored. Finally, theoretical analytic models are developed to characterize the nanofluidic transport properties observed in these systems. This work has tendered many groundbreaking advances in the field of separations and in nanofluidics. It will provide the groundwork for any future nanofluidic studies.

Contents

List of Figures

Chapter 1: Introduction:

The transport of fluids, electric currents and dissolved analytes in very small channels of nanometer size presents both practical and fundamental interests. At these dimensions (a few tens to a few hundreds of nanometers) the electric double layer that usually forms at the channel walls become comparable in size to the channel width. The relative wall surface to channel bulk volume ratio also increases and that facilitates a variety of adsorption effects. Hence, the fluid and the dissolved molecular and ionic species in nanochannels are subjected to a stronger interaction with the walls than those seen in common micro scale systems.

Transport phenomena in nanochannels will specific features that are not typical for larger micrometer and millimeter sized channels and capillaries. As mentioned previously, the electric double layer formed at charged walls occupies large parts of the nanochannels. This has an important impact on the fluid flow, streaming electric current though the channels, and transport of dissolved solutes, because it can shape the fluid velocity profile and spatial distribution of ions and charged analytes. These unique nanofluidic transport properties have yet to be fully explored in previous studies.

A detailed knowledge of these features is explored in the presented dissertation. By understanding how fluids, electric fields, and dissolved analytes behave in nanofluidic regimes, we can utilize these unique phenomena in order to fabricate highly efficient separation devices. Also by better understanding the novel transport phenomena involved

in nanofluidic regimes, we can achieve better optimization and performance of the different practical nanofluidic platforms.

1.1 Aim of Research:

The Specific Aims of this research are:

- *Provide the groundwork for study of fluid flow in nanofluidic devices.* Developing methods for fabricating these nanofluidic devices, and providing methodologies for performing experiments. This includes integrating macroscopic to nanoscopic regimes, exploring the various methods for inducing flow, and observing transport phenomena within nanofluidic conduits.

- *Perform separations within chip-based nanochannels.* This will take place on two fronts. First separations of dyes will be conducted to study the transport of simple molecules and to develop methodologies necessary for more complex analytes. Second separations of simple protein mixtures will be performed. This will include the use of surfactants to prevent adsorption and clogging of the nanochannels

- *Modify commercial capillary electrophoresis equipment to perform separations within a nano-diameter capillary*. A method of extruding a standard capillary such that it has a sub-micron inner diameter has been developed. We will modify a capillary electrophoresis machine to accommodate this type of capillary, and use

it to perform separations. This will utilize the UV adsorption detection and automated separation procedures that are standard in these conventional capillary electrophoresis devices.

- *Develop an analytic model that can be used to describe transport within these nanofluidic systems.* This incorporate the electrostatic potential within these devices with the continuum based fluidic transport principles to develop a basic model, which can be used to predict the transport of molecules within nanofluidic devices.

1.2 Literature Review: Molecular Separations in Nanochannels

A number of methods for forming well-defined nanofluidic systems have been developed of late expanding upon the concepts developed for microfluidic systems and exploring new phenomena unique to the nanofluidic regime. Many of these studies have been run concurrently along with the research presented in this proposed dissertation. This section reviews those studies that have sought to elucidate the effects of nano-confinement on molecular transport, and specifically on electrokinetically driven transport of molecular solutions. The transport of molecular solutes through channels of nanoscopic dimensions may be influenced by a number of factors, including the electrostatics of the channel, the solute and solvent, the solutes' molecular size and geometric and mechanical complexity, and the tendency of the solute to adsorb to the

channel walls. The possible exploitation of these effects in the development of new methods for high fidelity separation methods has been a primary driving force for investigations of molecular transport, especially in the case of isolation of high value biomolecules from mixtures. In this section, we review recent studies of transport of solutions through nanofluidic systems, specifically how transport was driven and monitored, and studies that have demonstrated possible new methods for molecular and biomolecular separations.

1.3 Dyes

1.3.1 Importance of studying dye transport

Until recently, very little has been known about the hydrodynamic properties of fluids confined within channels that are nanoscale in dimension. Recent advances in the manufacturing of devices on this scale have made experimental studies possible. The first step in the experimental exploration of nanofluidics is in the monitoring of the transport of simple molecular probes such as dyes, which can be used to infer velocity distributions of a fluid that is encapsulated within a nanochannel. Also, by studying dye transport researchers hope to obtain a realistic approximation of the motilities of more complex biomolecules within nanochannels.

1.3.2 Separations in Nanoporous Membranes

A number of nanofluidic devices (from nanoporous membranes to etched silicon nanochannels) have been employed to achieve separation of charged dyes. The permeability of a nanoporous nuclear-track-etched membrane (PCTE) is shown to be dependant on the charge of molecules being electrokinetically driven through the membrane as well as the ionic strength of the buffer used [1].

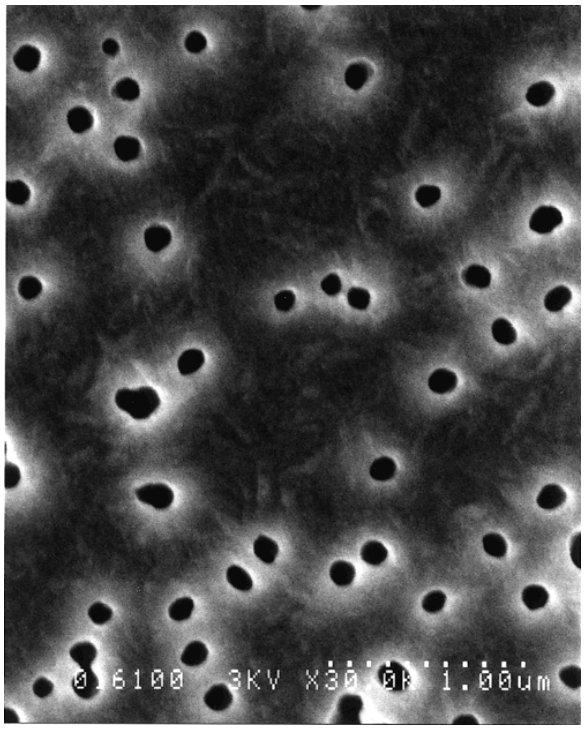

Figure 1: SEM of PCTE nonporous membrane [1]

Adjusting the ionic strength of the buffer proved to be an effective way to modify the length of the Debye Layer. This led to a decreased permeability of an anionic probe (Fl^{2-}) through the membrane in lower ionic strength buffers. This decrease in permeability of a charged molecule through the nanoporous membrane could be utilized to achieve separations based on the valence of the molecules. In addition, the electroosmotically induced permeability of a neutral marker (d-trytophan, no charge) was increased by 3.5x when the double layer occupies a significant portion of the pore cross section. A Spex fluorometer was used to monitor the flux of the fluorescent probes passing through the membrane.

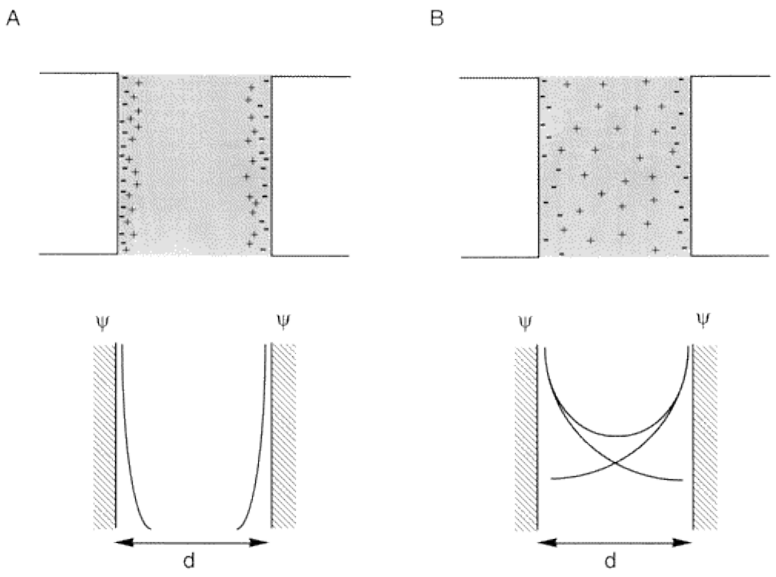

Figure 2: Schematic Diagram of the electrical double layer structures and electrostatic potential profiles that occur within a nanopore in cases where κa ≥ 1 and κa < 1. [1]

1.3.2.1 Nanochannels (Dye Transport)

Recently, arrays of nanochannels have been fabricated using existing semiconductor manufacturing techniques. These arrays can be integrated with microfluidic channels to achieve separations that are similar to those seen in standard gel electrophoresis systems. A two-dimensional separation chip was fabricated in Quartz integrating a microfluidic separation channel with an array of 900 nm wide (with a high aspect ratio) channels for further separations [2].

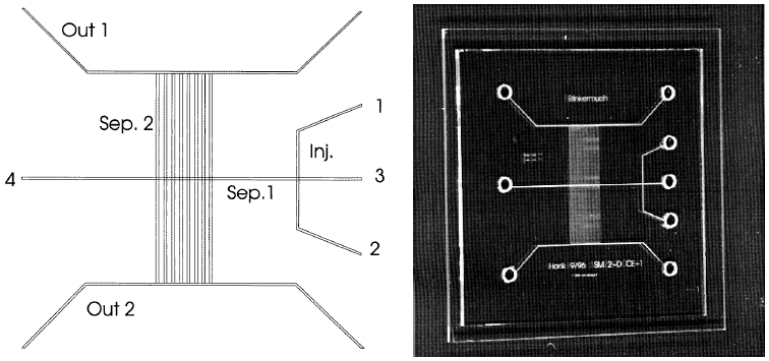

Figure 3: Layout of quartz-based chip, pointing out the different channels. Sep. 2 is the second dimension separation channel that consists of 500 parallel nanochannels. A photo of the completed chip can be seen on the right. [2]

Quartz was used to make detection possible while taking advantage of the native fluorescence of biological molecules when excited by UV light. Fluorescein was used to

fill the chip and test the UV detection capabilities, however separations of various dye mixtures or other biomolecules were not attempted.

In another study, controlled wet chemical etching was used to fabricate a chip that integrated channels that were nanometer in depth with microchannels in a standard 'T' configuration.

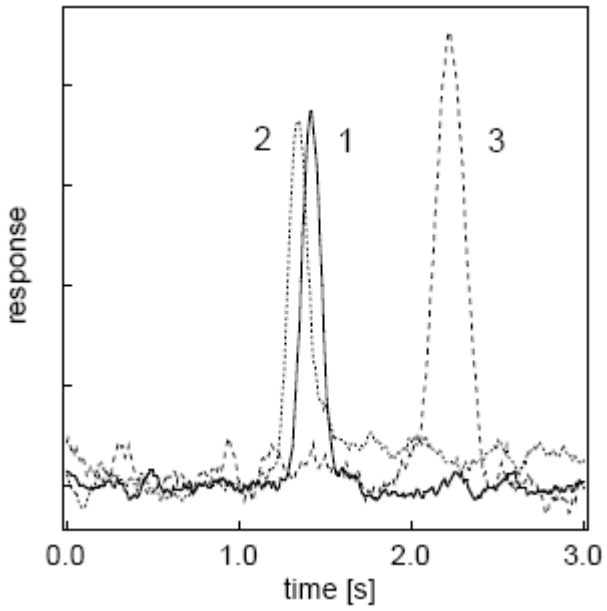

Figure 4: Temporal profiles measured within a 98 nm channel for double layer thicknesses of (1) 21.5 nm (2) 6.80 nm and (3) 2.15 nm [3]

Electrokinetically induced transport of a neutral dye (rhodamine B) within this nanochannel was measured for three different buffers with varying ionic strengths. [3] By adjusting the ionic strength of the buffer, it is possible to modify the length of the electrical double layer. The electroosmotic mobility of a neutral dye in the nanochannel chip was less than the mobility seen in a similar microchannel chip. This was attributed to the overlap, in nanochannels, of electrical double layers that originate from the channel

walls. This overlap prevents the electroosmotic velocity profiles from being fully developed resulting in slower electroosmotic velocities.

Similarly, an array of nanochannels was fabricated on a fused-silica chip using fast atom bean etching and hydrofluoric acid bonding methods [4].

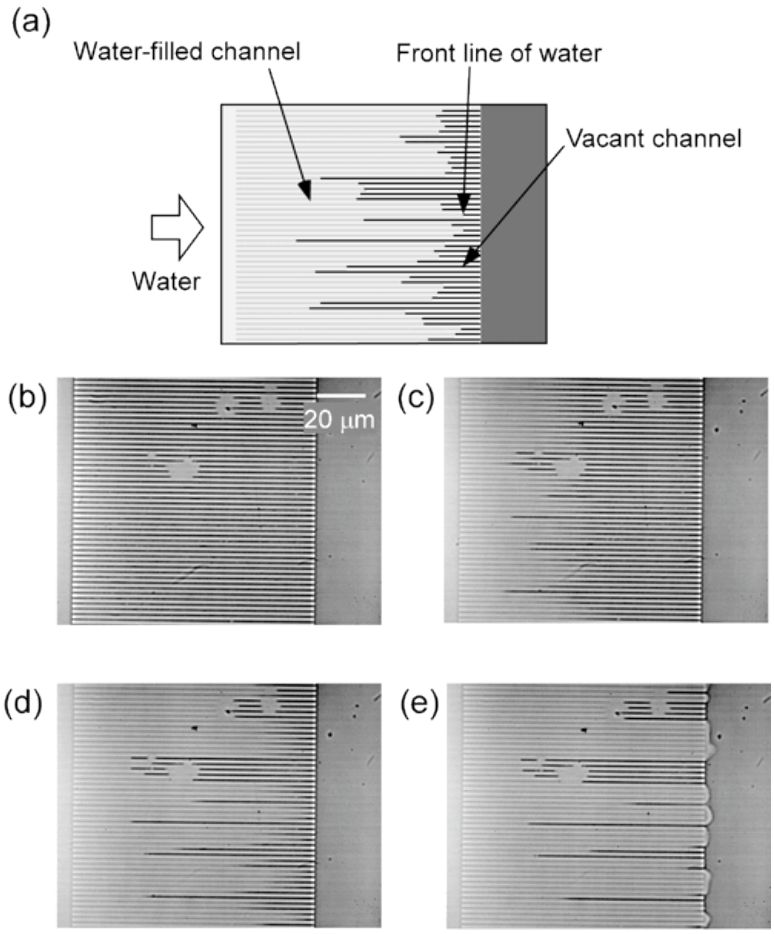

Figure 5: Optical microscope image of a 330 nm channel array being filled with water at an interval of 4 ms. [4]

Liquid introduction into the channels was studied for aqueous solutions of rhodamine 6G, rhodamine B, and sulforhodamine and their velocity due to capillary action was measured by time dependent fluorescence measurements on an optical microscope. A diagram of

the capillary action driven filling of the chip along with sample micrographs demonstrating the transport seen in a typical experiment can be seen in Figure 5. The measured velocities of the fluid fronts suggest that the fluids have lower dielectric constants (polarities) and higher viscosities than expected. It is hypothesized that this is due to the interactions between the surface charge of the fused silica and the hydrogen-bond network of water molecules.

1.3.2.2 Nanochannels (Dye Separations)

The next generation of experiments in these nanofluidic devices focused on the ability to utilize the unique properties of nanoconfinement to achieve highly efficient separations. Electrokinetic separation of fluorescently tagged amino acids were achieved in a chip system in which a three dimensional network of channels was set up consisting of two vertical microchannels that are connected by a nuclear track etched membrane containing an array of nanocapillaries [5].

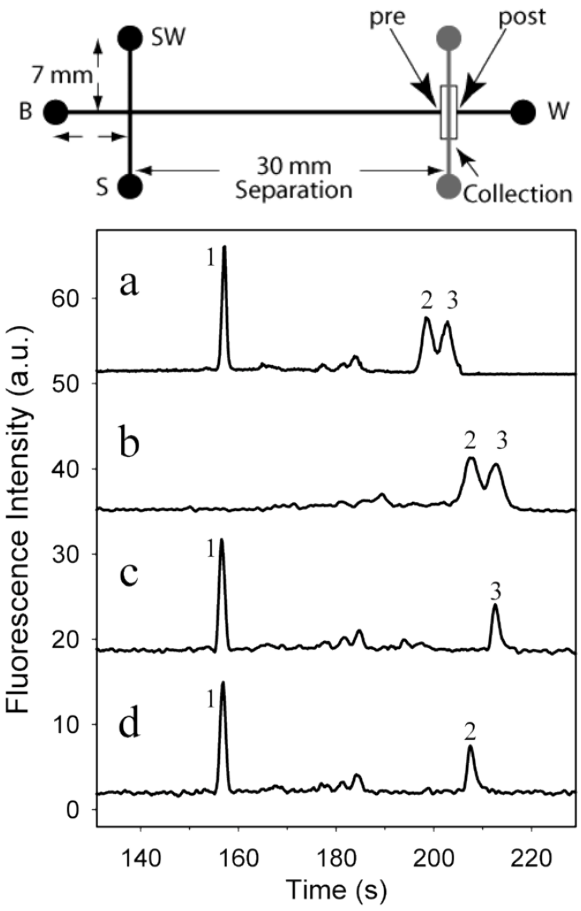

Figure 6: Schematic of separation chip and the electropherograms demonstrating the separation of specific analytes from the collection region of the chip. (a) is the case when the gate is not activated, (b-d) demonstrate the results after a specific analyte has been removed [5].

Separations occur in both micro- and nanochannel sections of this chip. By forwardly biasing the gate electrode, a specific amino acid complex is allowed to get into the nanocapillary array, and is removed from the main microfluidic separation channel. Thus that amino acid is not seen in the products of the separation conducted in the microchannel section. The fluorescence intensity vs. time graphs seen in Figure 6 convey this removal of specific fluorescent probes from the detection section of the chip. Single

spot or duel spot epi-illuminated laser-induced fluorescence (LIF) was used to monitor the transport of the FITC labeled peptides L-arginine and L-glutamate.

Building upon this concept of electrokinetic separation by ion valence, various configurations of nanochannel to microchannel geometries have been explored for their separation capabilities [6].

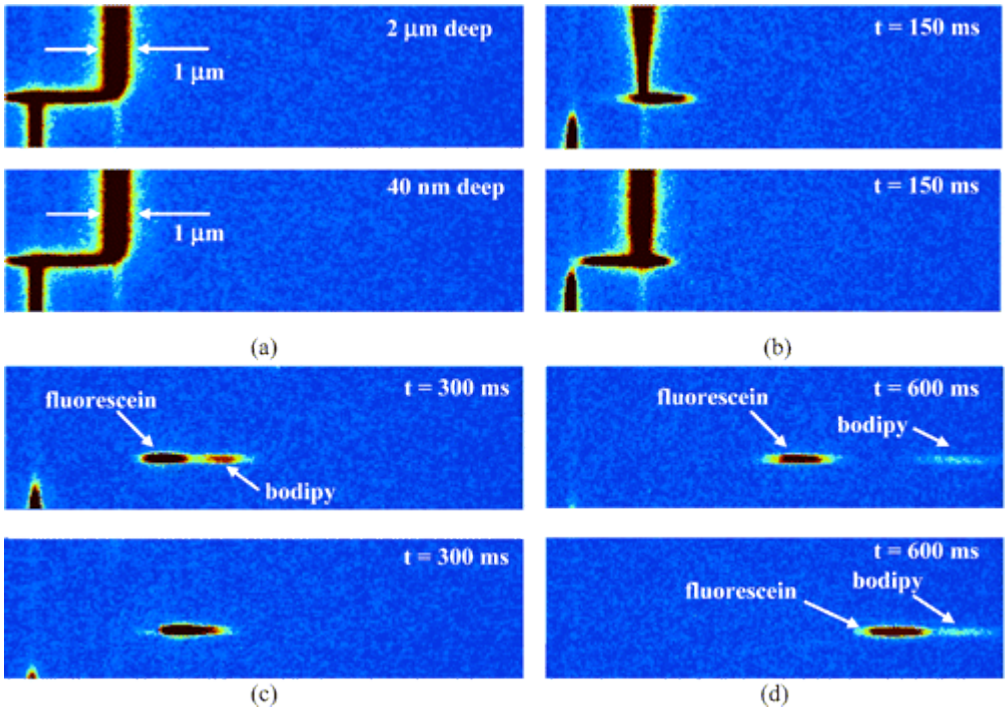

Figure 7: Fluorescence micrographs showing the separation of two negatively charged dyes Fluorescein (-2) and Bodipy (-1). The bottom image in each pair is 1 micron wide by 40 nm deep [6].

Conversely, valences and mobilities of molecules that were separated could be determined based on the their transport within these nanometer in depth channels. Separations of two negatively charged dyes Fluorescein (-2) and Bodipy (-1) were demonstrated. In other experiments, it was shown that the valences and mobilities of

unknown molecules could be determined based on the their transport within these nanochannels. Also it was seen that the area averaged electroosmotic velocity within these channels decreased as the amount of double layer overlap increased. This is also in agreement with the theoretically predicted results.

Because most of these chip fabrication techniques mirror those seen in the semiconductor field, many concepts of chip based circuit design could be harnessed in these separation systems. A nanofluidic transistor similar to MOSFET systems that are currently used in the microchip fabrication field was created to achieve further control of separations of charged analytes [7].

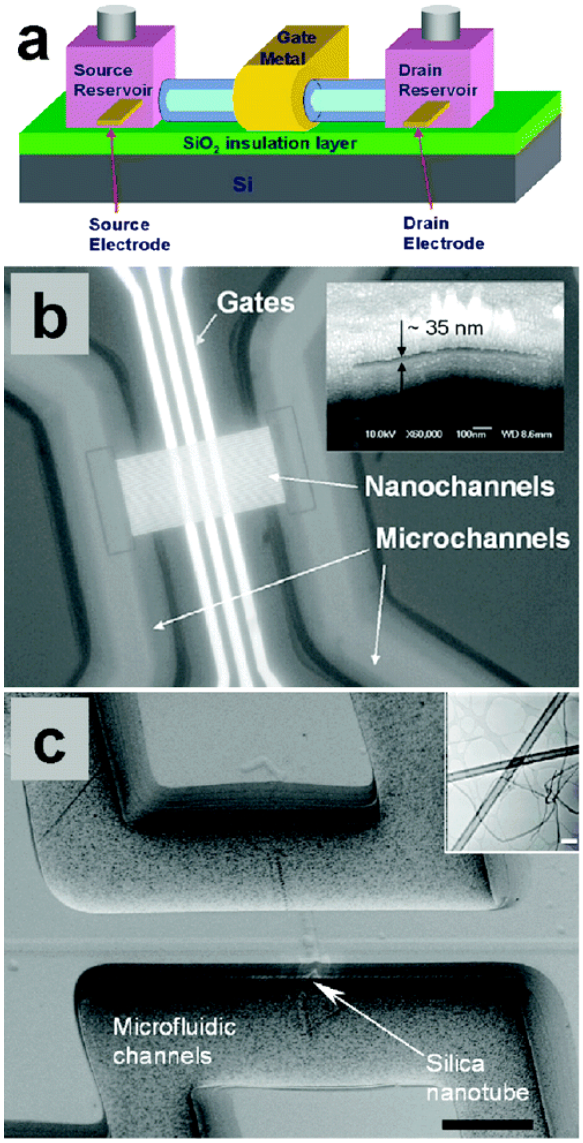

Figure 8: Schematic and micrographs of the nanofluidic transistor devices used in this study [7].

By applying an external bias to a chip based electrokinetic system, they were able to modulate the electrostatic potential from the walls of the chips. In nanochannels, where the Debye length is comparable in size with the channel thickness, this slight modulation should allow for localized changes in electrokinetically induced transport of molecules and ion concentrations. When a negative bias was placed on the array of 35 nm deep

channels, a negatively charged dye was repelled from the gating area. This could be utilized to selectively allow molecules of a certain charge into the nanochannel region, providing for a mechanism to perform separations. Conversely, when there was a positive bias of 50V place on the system, dye concentration was increased by a factor of 2. Single inorganic nanotubes that connect microchannels were also characterized for field-effect control of transport, showing similar results in conductance measurements as was observed in nanochannels.

1.4 Separation of biomolecules in Nanochannels

Researchers have begun to utilize these unique molecular interactions with narrow channels to perform separations of more complex biological molecules such as DNA and proteins. Currently, gel electrophoresis is the standard method to obtain these types of separations. However, this method has many drawbacks including the reproducibility of fabricating the gels, the need for relatively large sample sizes, the limited ability to run separations in parallel, and the high voltages and time needed to achieve separations. In using nanofluidic devices, researchers hope to improve upon all of these shortcomings.

1.4.1 DNA separations

DNA is usually one of the first biomolecules studied because of its linear geometry, and net negative charge. It is a relatively large molecule whose size could be comparable to the sizes of these channels. Currently, the bulk of nanochannel DNA separation experiments revolve around the concept of entropic trapping [8].

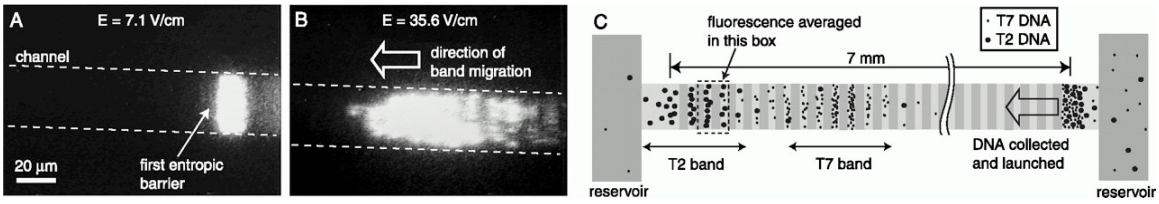

Figure 9: Micrograph and schematic showing the band launching and separation of DNA molecules of different length [8].

Han and Craighead fabricated a fluidic device with microchannels that are connected by narrower regions that were nanoscale in depth (Figure 9) When DNA molecules of different sizes are electrokinetically driven through these slender channels they are deformed from their random coil configuration. Because of this, the DNA molecules get trapped at the entrance of the constricted area of the chip. Therefore they exhibit slower mobilities, which are in turn dependant on the length of the DNA molecules. Longer DNA molecules travel faster through the system because they have a larger surface area in contact with the boundary of the nano-region, which increases the probability that they can enter. DNA molecules that ranged in sizes from 5000 to 160,000 base pairs were separated in 15 mm long channels with times up to an order of magnitude faster than

conventional slab gel separations. An example separation and a diagram of the separation mechanism can be seen in Figure 9. Separation efficiency decreased when attempting to separate these molecules under a higher electric field, however separations that were run in parallel in these chips were also demonstrated.

Because of this entropic barrier at the interface between microfluidic and nanofluidic channels, it is difficult to get DNA into nanoscopic regions at all. Cao et al. utilized a fabrication technique with combines optical and nanoimprint lithography to create a chip in which this there was a smooth transition from micro- to nanofluidic regimes (see Figure 10). [9] Fluorescently labeled DNA molecules were introduced into the nanochannel area of these chips more continuously (with less fouling of the chip), than in similar chips with less smooth transitions as seen in the micrograph shown in Figure 10.

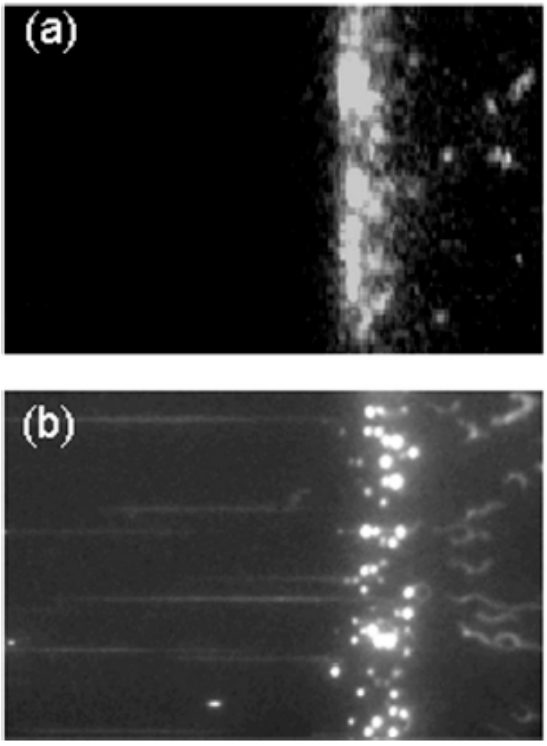

Figure 10: Micrograph of DNA entering the nanochannel region of chip. The top image demonstrates the inability of DNA to enter the nanochannel region in a chip with a step like change from micro- to nano- scale. The bottom image shows the stretched DNA able to get into the nanochannel section [9].

This entropic trapping experiment was further explored in a T-shaped device in which a microfluidic channel was fabricated with alternating shallow regions that were nanoscopic in depth [10]. Again, an entropic energy barrier, which arises from the difficulty in transporting molecules from a wider region to a more constricted region, enables size dependant separations to take place. First, a mixture of 3 SDS-protein complexes were separated based on their molecular weights in a channel that varied from 60 nm in the shallow areas to 300 nm in the wide regions.

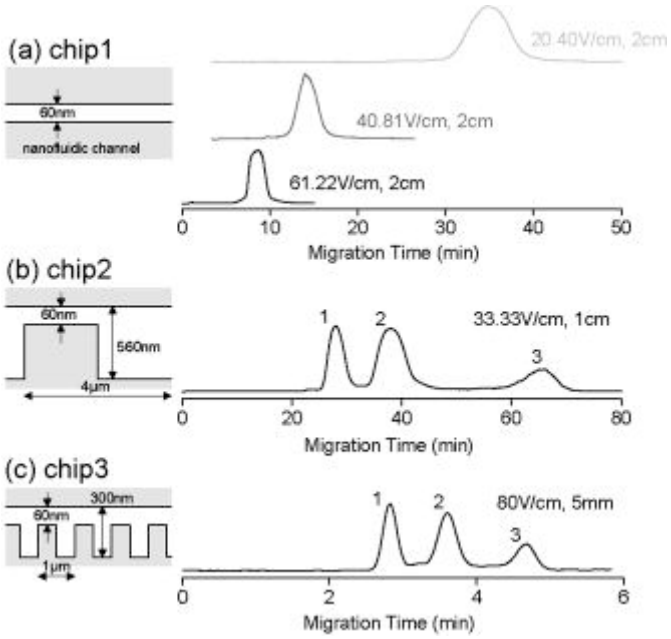

Figure 11: Comparisons of the separations seen in different configurations of nanofluidic chip [10].

The resulting separation took place in a length of 570 μm and a time of 30 s. Interestingly, the smaller proteins migrated faster, which is opposite to what was demonstrated in DNA separation experiments previously. DNA separations were also achieved in this system, separating 5 different lengths of DNA in ~10 minutes over a length of 5 mm. Different periodicities of narrow to wide regions were explored with shorter separation lengths achieved in chips with narrower and more periodic channels. The resulting separations seen in the different chip configurations are highlighted in Figure 11. Also of note, no separations could be achieved in straight nanochannels, indicating that they are due primarily to these entropic trapping effects.

1.4.2 Proteins

Separations of proteins prove to be a more difficult task than separations of DNA in these nanofluidic systems, possibly due to the high adsorption characteristics of proteins to silica. Therefore most of the studies of protein transport within nanochannels focus on developing protocols and methodologies for dealing with proteins as a part of a more complex nano- microfluidic system.

The intermediate step between separating protein mixtures and separating simple dye mixtures is to study the separations of peptides. Separations of peptide mixtures were achieved in an innovative shear driven nanofluidic system [11]. In nano- microfluidic systems there are two main methods for inducing current flow, using a pressure gradient and using electrokinetic pumping. Drawbacks of the use of pressure gradients include the inability to have higher resolution separations because of the parabolic velocity distribution, as well as the difficulty in integrating high-pressure systems from the macroscopic to nanoscopic level. Drawbacks of electrokinetic pumping include buffer incompatibilities with biological species (pH and ionic strength of buffer needs to be within a specific range), power supply issues, and electrolytic bubble formation. Also the velocity distribution of electroosmotic systems begins to become less flat in nanochannels, such that the resolution and throughput of the systems are decreased. Vankrunkelsven *et al*. created a shear driven flow by pressing together two fused silica plates, one of which had ~300nm deep nanochannels that ran along the length of the plate etched in it, and translating the flat plate at a constant velocity. A separation of the FITC labeled angiotension I and II mixture was obtained over a short time and space (0.2s and 2mm respectively). An example separation can be seen in Figure 12.

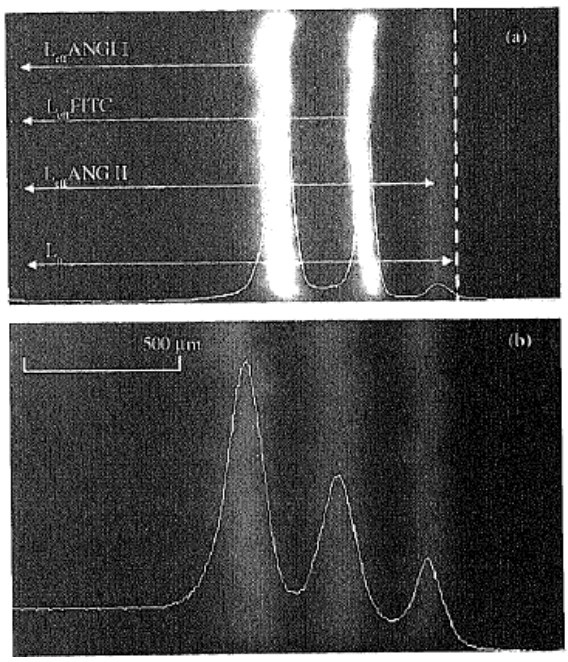

Figure 12: CCD image taken of the separation of the angiotension mixture for a wall velocity of 2 mm/s [11].

Protein transport was observed in a study by Karnik et al. that sought to build upon the results of the nanofluidic transistor concept, which was used to concentrate charged dyes. [12] The chip used connects two microchannel reservoirs with several arrays of nanochannels, which pass over a chromium plated gated region that allows for the application of an external bias.

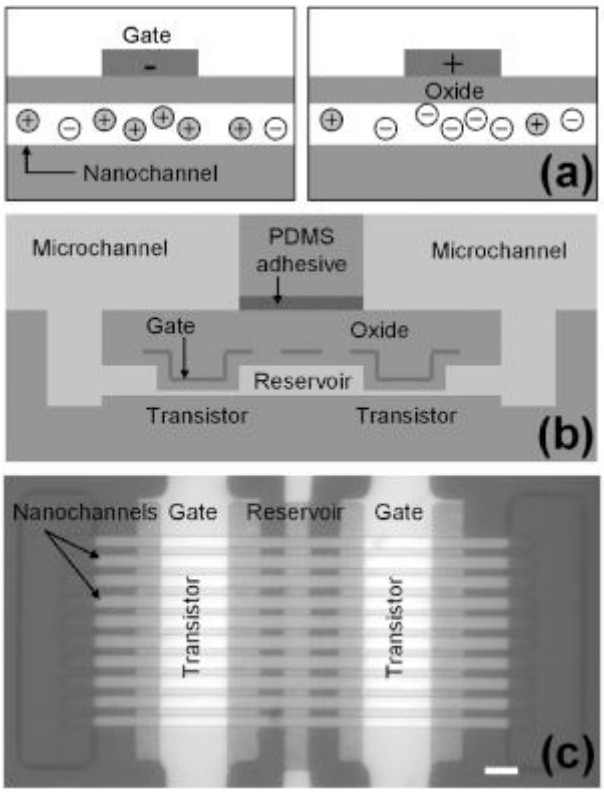

Figure 13: Nanofluidic transistor chip schematics and micrograph of fully fabricated device [12].

Fluorescence detection of Alexa 488 labeled avidin was used to measure the concentration changes. Gating voltages between –1 and +1 volts were used to modulate the electrostatic charge on the channel walls of the chip. When there was a –1 voltage placed on the system, the fluorescence intensity within the nanochannel reservoir increased. When a +1 voltage was used, the fluorescence intensity decreased, showing that the protein was repelled from the nanochannel region, demonstrating a field effect transistor (FET) like control. However, electrical breakdown of the insulating oxide layer on the chip occurred when the gate bias was about 2V, lowering the voltage that could effectively be used, thereby limiting the effectiveness of the FET.

Schoch et al. observed the separations of a protein mixture in a nanofluidic chip by utilizing the diffusion characteristics of charged molecules. [13] The diffusion of proteins within a silicon-based nanochannel is dictated by electrostatic interactions with the channel walls, which become more significant as the channel sizes become smaller.

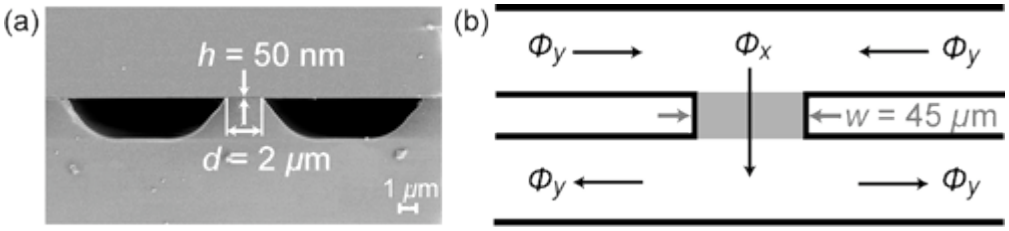

Figure 14: SEM of the cross section of chip used. Two microchannel regions are connected by a 50 nm deep nanochannel, which dictates the diffusion of the proteins [13].

The diffusion of proteins within a silicon-based nanochannel is dictated by electrostatic interactions with the channel walls, which become more significant as the channel sizes become smaller. A micrograph of a typical chip used in this study can be seen in Figure 14. Adjusting the pH of the buffering solution that fills the channel, thereby modifying the charge of the protein, can control these interactions. At low ionic strengths, the attraction/repulsion of charged molecules from nanoconduits causes them to distribute unevenly, in that way that allows for separations of these charged molecules. This phenomenon, known as the Donnan effect, has been explored in membrane separations, and is utilized there to separate lectin proteins with different isoelectric points and identical molecular weights. The resulting separation can be performed faster than those

seen in other common separation systems such as reverse-phase high-performance liquid chromatography.

Protein separations have also been conducted in microfluidic chips many times [14,15]. One of the challenges in using microfluidic devices is being able to detect the very small sample sizes involved. Therefore, preconcentration of samples becomes an important step in these systems, which is an area that can be addressed by integrating nanofluidic structures in these devices. A PDMS based microfluidic system has been constructed to perform concentration and separation of protein mixtures [16].

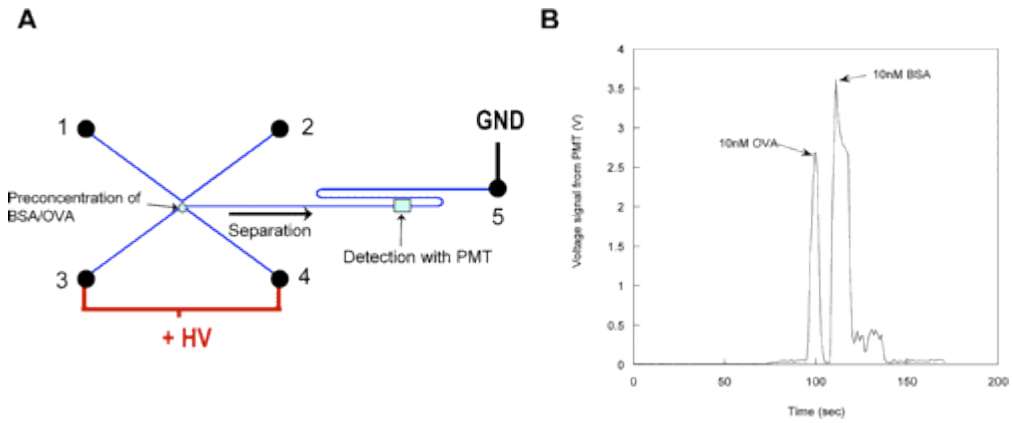

Figure 15: Left: Diagram of preconcentration/separation chip used in this study. Right: PMT readout showing two distinct bands demonstrating a separation of the two proteins [14].

Using conventional lithography, long microfluidic separation channels were created. By weakly bonding a section of flat PDMS along the microchannel, a nanofluidic section was created to perform concentration of the proteins. A diagram of this chip can be seen in Figure 15 (left). In nanochannels, a phenomenon known as the exclusion-enrichment

effect (EEE) becomes significant because the Debye length from the charge on the channel walls is comparable to the channel thickness. Therefore, negatively charged molecules tend to be excluded from the nanochannel region of the chip, while positively charged molecules are concentrated within. At a relatively fast speed (~30 min), concentrations of up to 10^6 could be achieved, and separations of two negatively charged proteins (bovine serum albumin and ovalbumin) could clearly be seen (see Figure 15). A positively marker charged dye, rhodamine 123, was used to confirm the effects of EEE in the nanochannel section.

In conjunction with the principles set forth in these studies, we developed our own platforms in which we can perform separations in a nanofluidic-based device. The fabrication and characterization of this device is discussed further in the following chapter.

Chapter 2: Fabrication of an integrated nanofluidic chip using interferometric lithography

2.1 Fabrication Introduction:

The study of molecular transport phenomena in fluidic channels with nanoscopic dimensions is at the current frontier of experimental and theoretical fluid dynamics. [17,18] Nanofluidic systems have a variety of applications including molecular separations, the manipulation and detection of biological molecules, and in sensor devices. [19,20,21,22] Until recently, the lack of suitable experimental systems has hindered the validation of theoretical studies and simulations that can predict the distinctive transport properties [23] and molecular dynamics [17,24] of nanofluidic systems. There are several design requirements for our device; the device must be amenable to high throughput production, allow for nanoscale patterning over large surface areas, facilitate the introduction of nanofluidic components with macro scale inputs, permit flexibility in design, and employ materials that are friendly with biomolecules.

2.2 Fabrication Background:

Electron beam (e-beam) lithography has been most widely used in producing nanofluidic systems with well-defined and controllable feature sizes. E-beam lithography allows for the creation of complex patterns and possesses extremely fine resolution.

[25,26] However, high-throughput fabrication is not practical with e-beam lithography due to its slow, serial processing nature that is not well suited for producing large areas of nanostructures.

Another approach is to use nanoimprint lithography. [21,27,28] This technique requires a mold to be formed first, usually by using e-beam lithography for nanoscale features [28,29] and incorporating optical lithography for larger features, such as integrated gradient structures. [28] The pattern is transferred to a thermoplastic polymer (e.g. polymethylmethacrylate) though heat and pressure [21,27,28] or into an ultraviolet (UV)-polymerizing liquid. [30] Nanoimprint lithography approaches are parallel, fast, and well suited for creating nanotextured patterns over macroscopic areas. However, a new mold must be created whenever a feature characteristic needs to be changed (e.g., pitch, channel size, gradient scale, etc.). Additionally, nanoimprint techniques have some difficulty in accommodating wide ranges of features size into a single pattern, and the issue of stamp lifetimes and drift in the resulting features has also not yet been fully explored. These issues may pose a challenge to high-throughput fabrication. [31]

2.3 Fabrication Approach:

We have based our manufacturing efforts on optical lithography, which is a well developed, reliable, and flexible fabrication practice. Interferometric lithography (IL), a maskless technique based on the interference of two or more coherent beams, allows on to inexpensively and quickly pattern nanoscopic features over large surface areas with

easily modifiable feature dimensions (e.g., pitch size and channel width). It is well suited for our goal of high-throughput manufacturing. [32]

While others have used traditional optical lithography for the fabrication of step-shaped, entropic trap, nanofluidic devices on silicon, these structures are only nanoscopic in the vertical dimension (created by controlled deposition or etching) with macro-microscopic transverse dimensions (controlled by lithographic pattern formation). [20] With our IL approach, two coherent beams of light with a wavelength λ are crossed at an angle 2θ, producing a regular interference pattern with a period, $d = \lambda/(2\sin\theta)$ as shown in Figure 16.

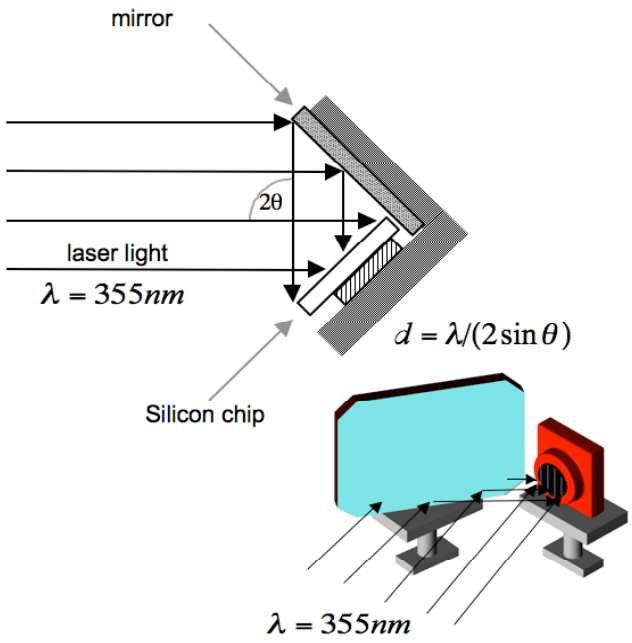

Figure 16: Schematic of interferometric lithography setup. UV light is directed towards the chip and on a highly reflective mirror. This creates a second coherent light source, producing an interference pattern, which is imaged on a silicon chip.

With an ultraviolet light source, one can easily obtain periods on the order of hundreds of nanometers and transverse pattern features in the sub- 100 nm ranges. This is well beyond the scales available from the traditional optical lithography approaches. Developments such as deeper ultraviolet sources and immersion techniques promise to extend these scales to sub- 100 nm periods and channel widths on the order of 10 nm. [33]

With this approach, nanochannels can be etched into silicon, rather than being pressed into plastic, what is done in imprint techniques. This is advantageous because silicon can be easily oxidized after etching, providing and inert, electrically insulating, and hydrophilic surface that can be chemically functionalized with silane chemistry. Also, a variety of etching processes and wafer-bonding techniques are available for silicon. This is important because most nanofluidic devices require one to seal the tops of a nanotextured surface to form nanoscopic tunnels rather than trenches. [20,21,26,28]

Interferometric lithography may be combined with traditional optical lithography to yield a wide range of characteristic sizes (mm to nm) on a single device. Here I will describe the fabrication of two variations of nanofluidic devices. The first is a large area nanochannel array chip, which consists of an oxidized nanoscale silicon grating that is capped with an anodically bonded Pyrex roof. Holes can be pre-drilled into this coverslip for convenient introduction of fluids. This type of device is analogous to traditional gel electrophoresis devices. The second device (referred to here as the T-Chip) contains a limited area of nanoscale features, integrated microchannels, and macroscopic reservoirs, using a convenient cross configuration that interfaces the nanofluidics to the macroscopic world and provides control mechanisms for fluid flow (others have also integrated their

nanofluidic channels with microfluidic channels, but in a simpler linear configuration). [26] Such cross configurations have been successfully and widely used in the study and manipulation of microfluidics, specifically in the formation of compositional plugs or bands of analyte. [34]

2.4 Fabrication Methodology

Blank silicon <100> wafers were used to fabricate these nanofluidic devices. Initially, these wafers were cleaved to a size of 3 x 4 cm^2 (alternatively, wafers that were circular with a diameter of ~2 inches were used to eliminate the time needed for measurement and cleaving, this also eliminated the waste that emanated from the cleaving technique). Batches of up to 15 chips could be processed by our method, limited only by the size of our in house equipment. These chips were then cleaned in piranha solution (1 part H_2O_2, 2 parts H_2SO_4 by volume), triple rinsed with de-ionized (DI) water, then cleaned again by dipping in hydrofluoric acid (to remove the native oxide layer and any remaining inorganic contaminants), and again triple rinsed in DI water. A 150 nm thick layer of XHRiC -16 (Brewer Science, Inc.) antireflective coating (ARC) was then spun deposited on the chip (4000 rpm, for 30 seconds) and hard baked at 175° C for 3 minutes. This was followed by spin deposition (4000 rpm, for 30 seconds) of a 200 nm layer of positive photoresist [SPR510a photoresist diluted by an equal amount of EC-11 solvent (Shipley, Inc.)] and soft baking at 95° C for 3 minutes.

The nanoscale features were then patterned using IL techniques. The exposure light source was the frequency-tripled (λ = 355 nm) output of a YAG-Nd laser (Infinity

40-100 Coherent Inc.). The laser beam is expanded and illuminates a right-angle assembly containing a mirror and a vacuum chuck to hold the chip. Although we have focused on pitches of 500 nm ($\theta \approx 26°$), the reflector assembly can be rotated to produce a variety of grating pitches.

After exposure, each sample was soft baked at 110° C for 1 min, developed using undiluted MF702 developer (Shipley, Inc.), and rinsed with water, leaving a photoresist grating. The developed chip was placed in an e-beam metal evaporator where a thin (35-40 nm) layer of Chromium was deposited. We then lifted off the remaining photoresist (and the Cr on top of it) using an airbrush acetone spray. This left a negative-tone Cr etch mask layer on top of the layer of ARC (which cannot be removed with acetone). A field emission scanning electron microscope (FE-SEM) image of one such mask is shown in Figure 17.

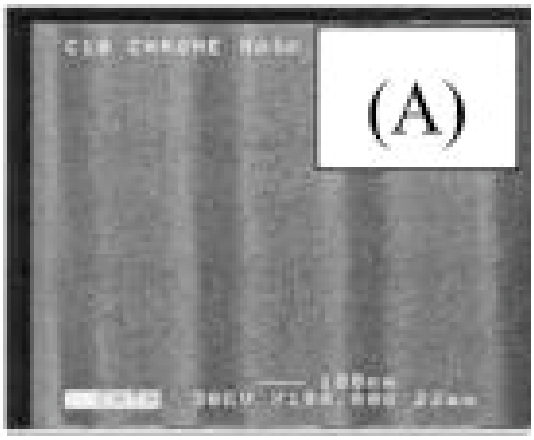

Figure 17: FE-SEM of a Cr etch mask after lift off procedure is done.

At this point either type of nanofluidic device can be created. Additional processing steps were used to prepare the integrated microfluidic channels before etching.

In our T-Chip device, we incorporated 200 μm microchannels and 2 mm diameter reservoirs with these nanofluidic areas. First the excess area of the nanofluidic grating was removed. A layer of 1.44 μm thick photoresist (AZ 5214-E, Shipley Inc.) was spun deposited (3000 rpm, for 30 seconds) on the chip on top of the Cr etch mask. The chips were then exposed with a rectangular exposure mask, using a conventional proximity aligner, developed, and baked (95° C for 10 min) to produce a protective layer over the area where we wanted to retain the nanochannel array, Figure 18(A). The chips were then placed in CEP-200 Cr etchant (Microchrome Technology) to remove the unprotected regions of the Cr mask. We then removed the protective photoresist layer with acetone leaving a small area (1 x 10 mm^2) on the chip with the Cr etch mask, see Figure 18(B). A 1.44 μm thick layer of AZ 5214-IR (Shipley, Inc.) resist was then spun deposited on the chip (3000 rpm, for 30 seconds), then exposed with a microchannel exposure mask, see Figure 18(C). This results in a chip with a microchannel etch mask made of photoresist and nanochannel etch mask made of Cr, see Figure 18.

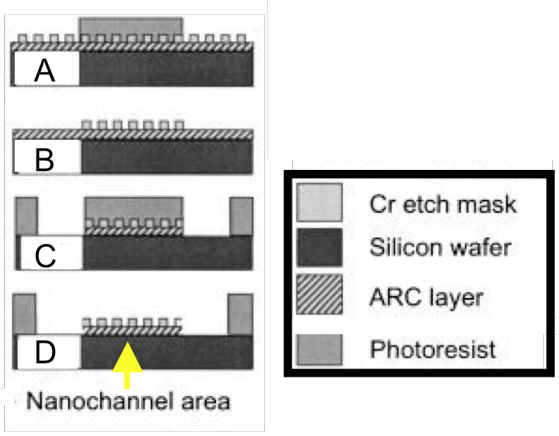

Figure 18: Fabrication steps schematic. (A) Protective photoresist section spun and developed allowing the removal of the Cr etch mask from unprotected areas. (B) Chip after Cr etch and acetone spray, leaving a small grating of Cr. (C) Chip after microchannel mask is fabricated using photoresist that is exposed and developed. (D) Chip ready for etching with exposed nanochannel etch mask.

The samples were then etched via a reactive ion etcher (RIE) using a mixture of O_2 and CHF_3. RIE was used because it provides a directional etching and allows us to create deeper troughs. The etched silicon gratings were cleaned with piranha solution to remove the remaining ARC layer, the excess Cr, and the residual polymer from the RIE process, see Figure 19(A). After cleaning, we then thermally grew a layer of oxide. The first method that we used involved simply placing the chip in a hot oxygen rich furnace for several minutes. In this method we placed several etched chips in a quartz tube furnace containing ultrahigh purity grade O_2 at 1100° C for several minutes, Figure 19(B). An insulating oxide layer was formed, however this layer was not vary dense and thus was not a very good insulator. A second method was developed in which we placed the etched and cleaned chips in a quartz tube furnace containing ultrahigh purity grade N_2, which was heated to 1100° C. While loading the chips, a small amount of ambient air was trapped in this tube providing the chips enough oxygen to still grow a layer of oxide. This process took about three times as long to grow the same thickness of oxide as the previous method, but oxide layers made with the second method proved to be denser and better insulators. In each method, we could vary the amount of time that the chips were

in the furnace in order to control the thickness of the resulting layer, thus providing us with a method for controlling the size of the channels.

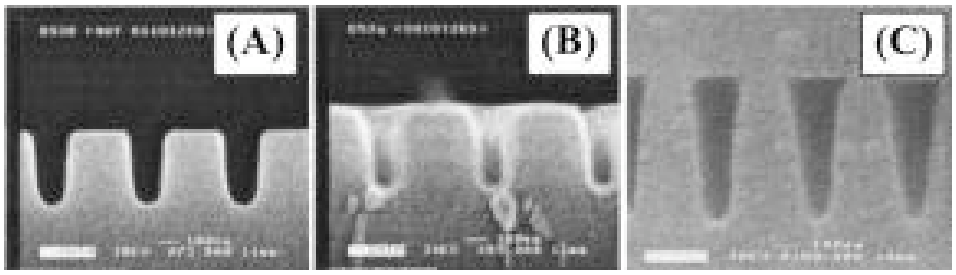

Figure 19: (A) Silicon chip after etching. (B) Same chip after oxidation. (C) Oxidized grating after anodic bonding step.

After etching and oxidizing, the chips were then capped with a 1 mm thick Pyrex No. 7740 roof using anodic bonding. These glass coverslips had a surface quality of 1.8λ [measured across a 2.54 cm diameter circle with a laser interferometer (Zygo, Inc.) at 633 nm]. For the T-Chips, the roofs were predrilled with four holes (~2 mm in diameter), located above the circular reservoirs at the ends of the microchannels. The roofs for the large area chips had four holes (3 mm in diameter) driller in a row on one edge to provide ports for convenient loading of analyte. Before bonding the Pyrex coverslips were cleaned with piranha and triple rinsed. The oxidized chip and its coverslip were then assembled in a bath of ultra pure DI water, aligning the predrilled holes with the reservoirs. The chips were then dried, forming a weak bond between the chip and coverslip. This made the rest of the bonding process easier, and reduced the amount of

contaminants that could be introduced during the bonding process, which took place outside of the cleanroom environment.

During bonding, the bottom electrode of the bonding apparatus was the grounded metal surface of a hot plate, on which the chip-coverslip assembly was placed. The upper electrode was a small aluminum block that was placed on top of the Pyrex roof and connected to a high voltage power supply. Longer strips of aluminum could also be used to parallelize this process and bond several chips at one time. We raised the temperature of the hot plate to 380° C before charging the capacitor structure. We would typically increase the capacitor voltage slowly until the current reached a value of 1-2 mA, then allow the current to decay to ~0.5 mA (indicating the formation of a space charge blocking layer) before further increasing the voltage. We used as large of a voltage as possible while avoiding arcing between the electrodes (typically 800-1000 V). We monitored the current flow through the system until it decayed to ~100 μA before shutting off the heating element and allowing the samples to cool. The voltage was decreased to zero when the temperature dropped below 150° C. A FE-SEM image of a bonded chip cross section is shown in Figure 19(C).

2.5 Fabrication Results:

Once these test chips have been fabricated, we had to prove the feasibility of inducing fluid flow within nanoscale conduits. Several methods were examined, including using capillary pressure, applied pressure, and electrokinetic means for inducing flow.

For the working fluid we used a buffer solution that is commonly used in traditional gel capillary electrophoresis setups. We prepared a solution of standard Tris/glycine electrophoresis buffer (0.24 mM Tris and 1.92 mM glycine pH 8.3). This buffer is known to be compatible with biological molecules. Before introducing the buffer into our chips systems, it was filtered through a 0.2 μm filter to remove general particulate contaminates, and then degassed under vacuum for at least 3 hours to reduce outgassing during the electrokinetically controlled fluid transport.

We used florescent markers to examine the flow within these chips. A 5 mg/mL suspension of Alexa Fluor 532C5 maleimide (Molecular Probes) was prepared in 1.5 mM Tris HCl buffer ph 8.8.

2.5.1 Fluid Flow in Large-area nanochannel array chip

We mounted the large-area nanochannel array chip into a Teflon chuck with reservoirs at each end of the chip. Platinum wire mesh electrodes were inserted into the far ends of both reservoirs (~3 cm from the chip edge). Poly(dimethylsiloxane) (PDMS) was used to secure the chip to the chuck and seal the system both for fluid flow and to electrically isolate the two reservoirs. A schematic can be seen in Figure 20(A). The assembly was imaged using an upright, laser scanning confocal microscope (Axioskop using an LSM5 scanning head, Zeiss, Inc.). The fluorescence output passed through a long-wavelength pass optical filter (560 nm cut off). Approximately 2 μL of the Tris/glycine solution was introduced into the nanochannel array though the hole cut in the Pyrex coverslip. After capillary action caused the buffer to move ~ 5mm though the nanochannels, we added ~5 μL of the Alexa 532 solution to the injection hole. The flow

of the dye within the nanochannels was then imaged as shown over a 30 second period in Figure 20(B). The average fluid velocity due to capillary forces was measured at 12.2 ± 0.6 μm/s (the location of the dye front was obtained at specific time intervals at various positions along the array). There appeared to be no noticeable dye movement across the nanochannel array, demonstrating the high degree of quality in our fabrication and bonding. This also proved that the chips could be filled with liquid, something that had been in question because of the small volumes of the nanochannels.

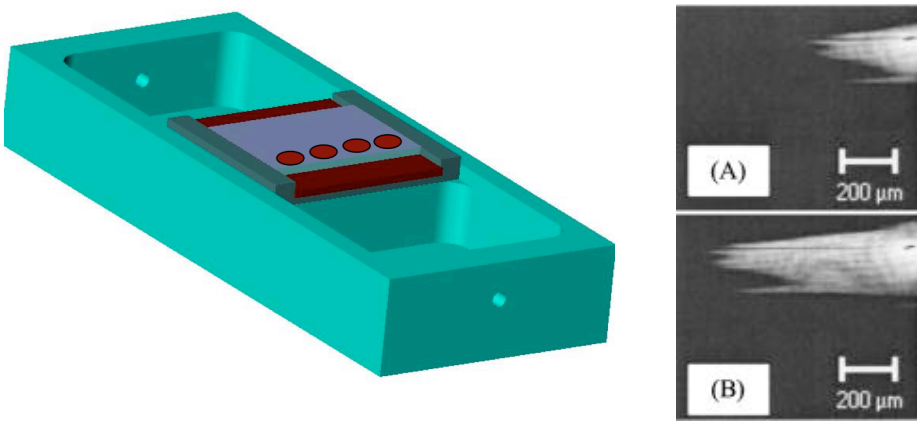

Figure 20: (left) Schematic of large area chip test setup. Chip is secured in Teflon chuck via PDMS. (A, B) Confocal images of capillary driven fluid motion in large area type

chips. The difference in time between images is 30 seconds. Bright regions denote portions of the array filled with Alexa 532 dye, while the dark regions are empty, air filled channels.

To test the feasibility of using electrokinetic means of inducing fluid flow, we first filled one reservoir with buffer up to the chip level. Once the buffer level reached the surface of the chip, the nanochannels filled with fluid via capillary action. This filling could be observed by the naked eye or with brightfield microscopy (since filled channels have a different index of refraction than empty ones, the color of the chip changes as the nanochannels become filled), see Figure 21.

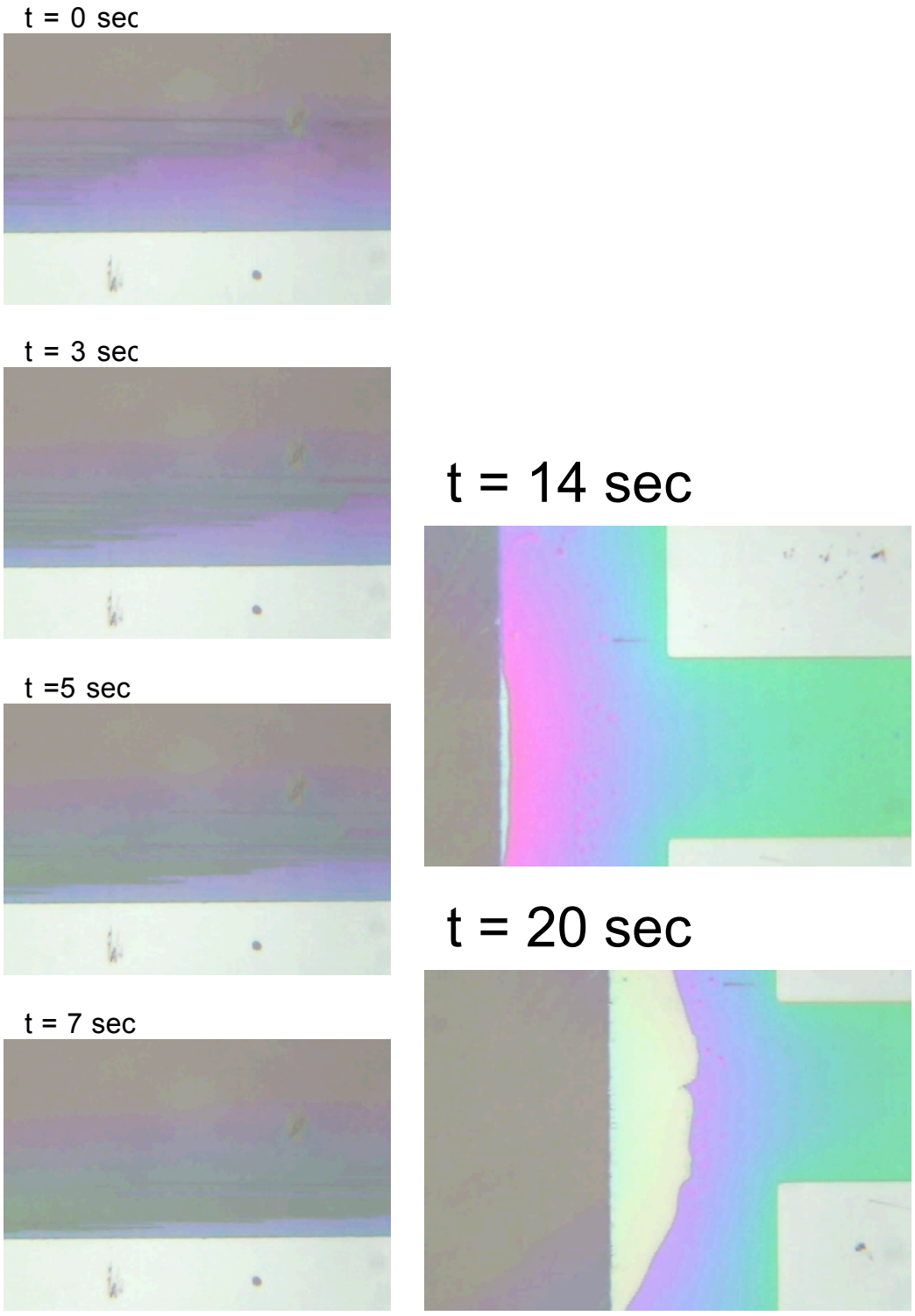

Figure 21: Bright field micrographs of buffer filling nanochannel array. Left: The channels change color as the nanochannels become filled. Right: The microchannel begins to fill after the buffer has migrated through the nanochannel array.

Once the buffer reached the end of the nanochannel array, the second reservoir was filled with buffer. We then inserted 1 μL of Alexa 532 dye into one of the four holes on top of the chip and a 50 V bias was applied via the electrodes. Figure 22 shows the progression (due to electrophoresis) of the negatively charged Alexa 532 dye over a period of 150 seconds. Because of the high ionic strength of the buffer, these systems have a short Debye length. The average velocity was measured to be 0.77 ± 0.03 μm/s.

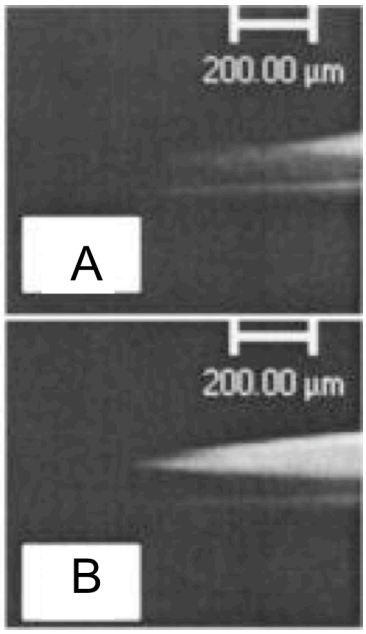

Figure 22: (A) Large area chip after the introduction of dye and filling with buffer. Bright area is the channel section that is filled with dye, while the dark regions are channels filled with buffer and no dye. (B) Taken 150s after the application of bias.

2.5.2 Fluid Flow through T-Chip

Before introducing liquids into these chips, polyetheretherketone (PEEK, Upchurch Scientific, Inc.) reservoirs were attached to the Pyrex coverslip over the predrilled holes. We loaded one of the integrated chips with liquid via capillary action. First, we loaded 50 μL of buffer into the South reservoir (as defined in Figure 23). We monitored the flow of water through the microchannel and nanochannel regions by eye until the water had reached the north end of the nanochannel array. At that point , 50 μL of buffer was introduced into the East reservoir, filling the remaining three microchannels. After allowing the system to equilibrate for 30 minutes, Tris/glycine buffer was added to the remaining reservoirs bringing the height of the buffer in each reservoir to the same level. We inserted platinum wire electrodes into all four reservoirs and attached them to 3 independent DC power supplies; the West reservoir acted as the common ground. The fluid flow was again imaged with a laser scanning confocal microscope.

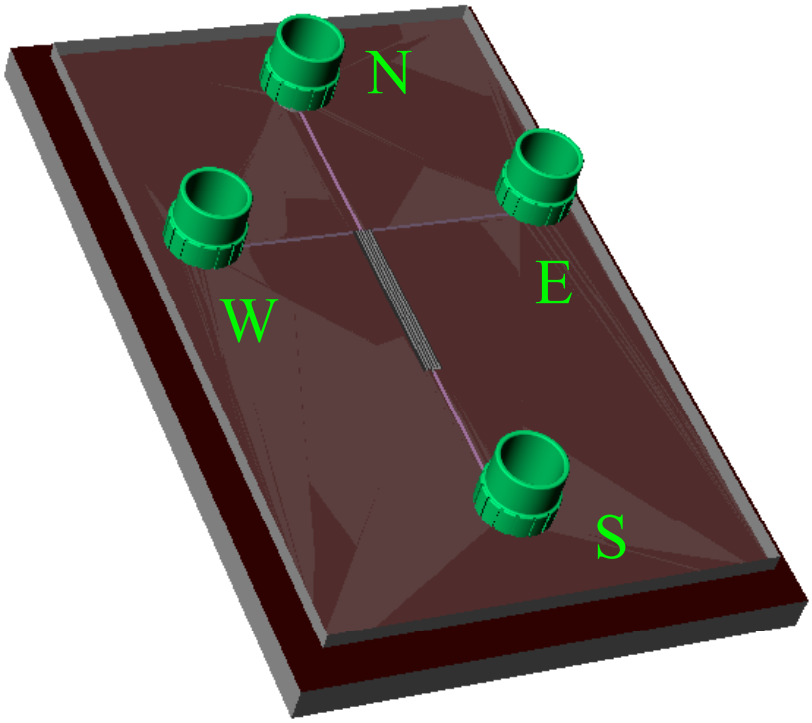

Figure 23: Schematic for T-Chip showing the compass direction labeling of specific reservoirs and the attachment of PEEK reservoirs.

We introduced 5 μL of Alexa 532 dye into the Ease reservoir and biased its electrode at -100 V. The remaining electrodes were at a ground potential. The negatively charged dye moved towards the center of the chip, entering both the nanochannel area and the microchannel connected to the North reservoir as seen in Figure 24(A-B). We then changed the bias of the North reservoir to -100 V. This flushed the dye out of the North microchannel and pinched off a plug of dye in the nanochannel array directly across the North microchannel, as seen in Figure 24 (C-D). We can see a clear

progression of the plug down the nanochannel array for ~20 seconds which was measured to be moving at a rate of 26.5 ± 0.9 μm/s.

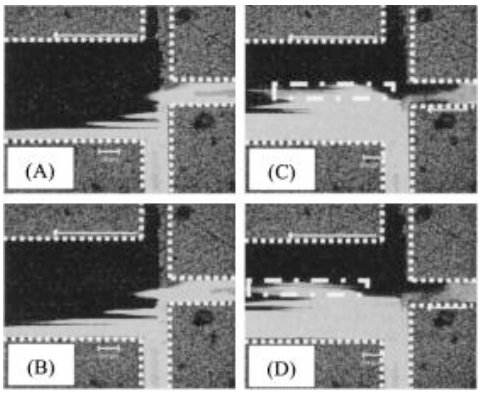

Figure 24: Confocal microscopy of electrokinetically driven flow within the T-Chip. The channels are outlined for clarity because of the high amount of background chip fluorescence. (A) The electrode for the lower (east) channel is biased at -100 V while the other 3 remain grounded. Electrophoresis causes the dye to flow through the lower microchannel towards the top part of the picture. Dye enters the nanochannel array as it reaches that section of the T-Chip. (B) Taken 60 seconds later, showing that dyes has progressed down the nanochannels. (C) After the right electrode (north) is biased at -100 V. The lower channel remains at -100 V, and the other two remain grounded. The dye has been flushed out the right hand side microchannel ad pinched off a slug of dye, which is outlined with broken lines. (D) Taken 20 seconds later, showing the progression of the slug through the nanochannel array.

2.6 Fabrication Discussion:

We have demonstrated that these nanofluidic chip designs are suitable for experiments in studying electrokinetic motion in nanoscale channels. It is interesting to note that we were able to achieve much higher electrophoretic velocities in the integrated T-Chip. This is due, in part, to he difference in nanochannel length. The length of the nanochannel area of the integrated chip is about 1/3 of the length of the sealed nanochannel in the large area chip. The microchannels are les than 2/3 of the length of the sealed channels, and have a lower resistance (due to the larger cross sectional area), resulting in a larger electric field across the nanochannels for a given electrode bias voltage. This coupled with a twofold higher electrode bias, could account for a factor of 6 difference, less than the facto of 32 observed. Another contributing factor may be the difference in buffer concentration between the two solutions. It is also interesting to note that the fluid velocities due to capillary action in the large area chip are also quite fast (approximately half of the electrokinetically induced velocities in the T-Chip). Further investigation is necessary to full characterize the fluid-flow characteristics in these nanochannel samples.

Application of 100 V to the large area nanochannel chips quickly resulted in a drop in current across the chip and an eventual cessation of electrokinetic motion, which is caused by the breakdown of the oxide layer allowing current to flow through the chip. Outgassing of the solution was also a major problem. Rapid generation of bubbles could be seen at the edge of the nanochannels. These effects were also seen in the microchannel regions of the T-Chip, but not witnessed directly within the nanochannel array. There is

doubt that bubbles can be present within nanochannels without being reabsorbed into solution because of the tremendous pressures involved.

2.7 Fabrication Conclusion:

We have created functional nanofluidic chips based on an all-optical lithographic process with feature sizes ranging from tens of nanometers to 2 mm on a single chip. Interferometric lithography is the basis of the nanochannel fabrication, and allows for flexible nano-patterning of silicon chips over large surface areas. Traditional optical lithography provides the ability to integrate suitable microfluidic structures for interfacing with the nanochannels and controlling fluid flow as we have demonstrated with cross-type microfluidics. Our techniques are suited to high-throughput manufacturing, providing flexible nano-texturing over large areas, and can produce a broad range of feature size on a single chip. They allow one to use inert and hydrophilic nanotextured surfaces (oxidized silicon with glass roofs) that are compatible with electrokinetic studies.

Future fabrication work could involve the addition of integrated microelectrodes to the chips, various nanochannel pitches, two-dimensional patterning of the nanochannels (e.g., introducing gradients in channel widths), and adding additional switching capabilities to form more complex micro/nanofluidic arrangements. This opened the door for our experimental work including the detailed parametric studies of electrokinetic motion and flow rates, and the investigations of separations of biomolecular species within the nanochannel devices. The first of which can be seen in the following chapter.

2.8 Fabrication Acknowledgements:

This work could not have been done without the efforts of Dr. Michael J. O'Brien, and Dr. Steven R. Brueck, who are pioneers in the field of interferometric lithography. Thanks to David Burckel and Andrew Frauenglass for advice and help with IL, and Beth Fuchs for fabrication advice across a broad variety of topics. Support for this work was provided by the ARO/MURI in Deep Subwavelength Optical Nanolithograhy, the Mission Research Corporation in subcontract from the Air Force Research Laboratories, the Keck Foundation, and the National Science Foundation. Images were obtained from microscopes provided by the Keck Nanofluidics laboratory and the UNM Cancer Center.

Chapter 3: Dye Separations - Electrokinetic Molecular Separation in Nanoscale Fluidic Channels

3.1 Dye Separations Introduction:

This section presents a study of electrokinetic transport in a series of integrated macro- to nano-fluidic chips that allow for controlled injection of molecular mixtures into high-density arrays of nanochannels. The high-aspect-ratio nanochannels were fabricated on a Si wafer using interferometric lithography and standard semiconductor industry processes, and are capped with a transparent Pyrex cover slip to allow for experimental observations. Confocal laser scanning microscopy was used to examine the electrokinetic transport of a negatively charged dye (Alexa 488) and a neutral dye (rhodamine B) within nanochannels that varied in width from 35 to 200 nm with electric field strengths equal to or below 2000 V/m. In the negatively charged channels, nanoconfinement and interactions between the respective solutes and channel walls give rise to higher electroosmotic velocities for the negatively charged dye than for the neutral dye, towards the negative electrode, resulting in an anomalous separation that occurs over a relatively short distance (< 1 mm). Increasing the channel widths leads to a switch in the electroosmotic transport behavior observed in microscale channels, where neutral molecules move faster because the negatively charged molecules are slowed by the electrophoretic drag. Thus a clear distinction between "nano-" and "microfluidic" regimes is established. We present an analytical model that accounts for the electrokinetic transport and adsorption (of the neutral dye) at the channel walls, and is in good

agreement with the experimental data. The observed effects have potential for use in new nano-separation technologies.

Elucidation of phenomena associated with flow of liquids through conduits of nanoscale dimensions remains an important scientific goal as nanofluidic devices receive increased attention. Specifically, the development of chip-based nanofluidic systems for molecular (especially biomolecular) separations based on nanoscale phenomena including entropic trapping [35] and shear-driven chromatography [36] has recently received intense interest. In addition to a limited number of experimental efforts [37,38,39,40,41,42] several important theoretical studies have sought to clarify the effects of nanoconfinement of fluids on the transport of ions and molecules in electrokinetic flows. [43,44,45] For example, a recent study by Qiao and Aluru concluded that effects resulting from the non-continuum nature of electrokinetic flows in nanoscopic pores are associated with varying fluid viscosity very close to the pore wall. [46] Further, with this correction, electroosmotic velocity profiles more than a few molecular layers away from solid surfaces are in reasonable accordance with the continuum theory. [47,48]

The goals of this study are (i) to develop methodologies for investigation of electrokinetic transport in nanoscale channels (averaged across many nanochannels) using confocal scanning laser microscopy, a widely available far-field technique, and (ii) to explore the potential use of nanoconfined electrokinetic transport in molecular separations. For the purpose of this study, we use the term nanoconfinement to refer to a situation in which electrical double layers that form in the presence of charged channel walls (Debye screening layers) extend into the channel significantly, thus representing a significant percentage of the channel width, and thereby effecting the nature of the

electroosmotic velocity profiles. For solutions with ion concentrations relevant to separation of biomolecules, this leads to more complex electroosmotic velocity profiles than the usual "plug-like" flow observed in capillaries of larger sizes. [48]

Charged solutes in electrolyte solutions that are electrokinetically driven through channels with nanoscale widths exhibit unique transport characteristics that may provide significant technological benefits because most biomolecules (DNA, proteins, peptides) are charged, or can be complexed with charged surfactant molecules. The significant alteration of the velocities of these species in electrokinetic and pressure-driven flows through channels of nanoscopic widths may enable efficient separations over short lengths not possible in channels of macroscopic or even microscopic width.

3.2 Dye Separations Fabrication

We used silicon-based T-chips, integrating an array of parallel nanochannels with microchannels for fluid control and macroscopic injection ports, to study the electrokinetic transport of fluorescent dyes in nanochannels (Fig. 1A). [49] The different T-chips incorporate nanochannels that range from 35 to 200 nm in width in the plane of the chip, while being deep enough to allow significant molecular throughput and to provide large enough signals for facile detection by laser-induced fluorescence microscopy. The high aspect ratio of the channels is amenable to description by relatively simple analytical models that allow interpretation of the results of our experimental system. Other advantages, as well as fabrication details have been discussed elsewhere. [49] The nanochannel section (1 mm in width and consisting of ~2000 parallel

nanochannels) is located within Arm 3 of the T-Chip (Figure 25A), and originates at the intersection of the microchannels and extends 1 cm down Arm 3. A cross-sectional scanning electron micrograph of a small number of nanochannels in one of the T-chips used for this study is shown in Figure 25B. In this chip, the channels are approximately 50 nm wide by 500 nm deep, and are on a 400 nm pitch. The channel width is sufficiently narrow to result in interaction between the diffuse double layers extending from opposite sides of the channel walls. Fluorescence from the dye molecules in the fluid is monitored through the transparent lid using confocal microscopy. While the details for the flow profiles in the individual nanochannels are below the resolution limit of conventional optical microscopy, average velocities of dye fronts can be monitored and provide insight into the electrokinetic transport mechanisms in the nanochannels.

3.3 Dye Separations Experimental Results:

Electrokinetic separations used a buffer containing 0.25mM *tris*-(hydroxy)aminomethane hydrochloride and 1.92 mM glycine at pH 8.8 (viz., a 1/100 dilution of the standard poly(acrylamide) gel electrophoresis buffer). The ionic strength of this buffer was estimated to be ~0.35 mM as calculated from the pK_as of each salt. At this ionic strength we estimate the magnitude of the Debye screening length ($1/\kappa$, see below) to be ~16 nm. The buffer was filtered through a 0.2 μm filter to remove particulate contaminants and then degassed under vacuum for at least 3 hours. Solutions of dyes (rhodamine B (MW = 479 Da) and Alexa 488 maleimide (MW = 720 Da), Molecular Probes Inc.) were prepared in this buffer, each at a concentration of 5 mg/mL.

At pH 8.3, rhodamine B is neutral and Alexa 488 maleimide has a charge of –2. [50] The addition of Alexa contributes a negligible increase in the ionic strength of the bulk solution.

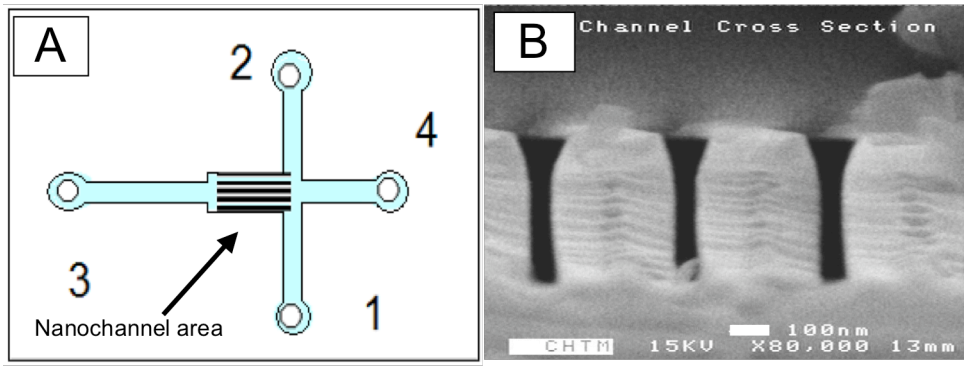

Figure 25: (A) Top view (schematic) of the integrated chips. The holes are numbered for reference, and nanochannel area is noted. The channels are 3 cm long from well 3 to well 4, and 2 cm from well 1 to well 2. (B) SEM image of the cross section of the nanochannel array (50 nm wide nanochannels) in a chip taken after experiments were performed showing a Pyrex lid bonded to the oxidized silicon trenches to form channels.

Electrode 2 (see Figure 25A) was grounded, while the remaining 3 electrodes were attached to the outputs of three separate DC power supplies. The chip was filled with buffer (no dyes) via capillary action from well 3 and placed under an upright, laser-scanning confocal microscope (Zeiss Axioskop with an LSM5 scanning head). Ten μL of a 1:1 mixture of the two dye solutions were introduced into well 1, and initially Electrode 1 was set to +30V relative to Electrode 2 (Electrodes 3 and 4 were set to 0V) so that the solution moved from well 1 towards well 2 by electroosmosis in the microchannel.

Separation of the two dyes was not observed in the microchannels during this step. Once the dye mixture (as monitored by fluorescence microscopy) reached the T-intersection, Electrode 1 was set to 0V and Electrode 4 was set to +30V so the fluid flowed towards well 3 through the nanochannels via electroosmosis. Dye velocities were obtained by tracking the time evolution of the dye fronts through the nanochannel array. [51] At least thirty measurements of dye front velocities, throughout the cross section of the nanochannel arrays, were averaged to obtain the velocity corresponding to a given field strength.

Figure 26 presents laser-induced fluorescence micrographs that demonstrate differential transport of the two dyes in channels with widths of ~50 nm (left) and ~200 nm (right). Dye fronts in the array of 200 nm-wide channels are observed to be more uniform. The smaller channels are more of a fabrication challenge and likely have larger percentage in width deviation leading to the observed variations in dye front uniformity. We performed a study to characterize the uniformity of the channels in which several SEM cross sections of the nanochannel arrays were taken at different places in the array. We measured the inhomogeneity of the channels to be approximately 4-6% deviation in 50 nm channels and a much smaller percentage deviation in wider channels. This inhomogeneity in the channel widths should not affect the data we collect because our measurements at low magnification average over quite a few channels (~100), which are spaced by less than the optical wavelength. Also the dye velocities for each chip and EO voltage were measured at different locations within the nanochannel array, and were not observed to differ greatly from region to region.

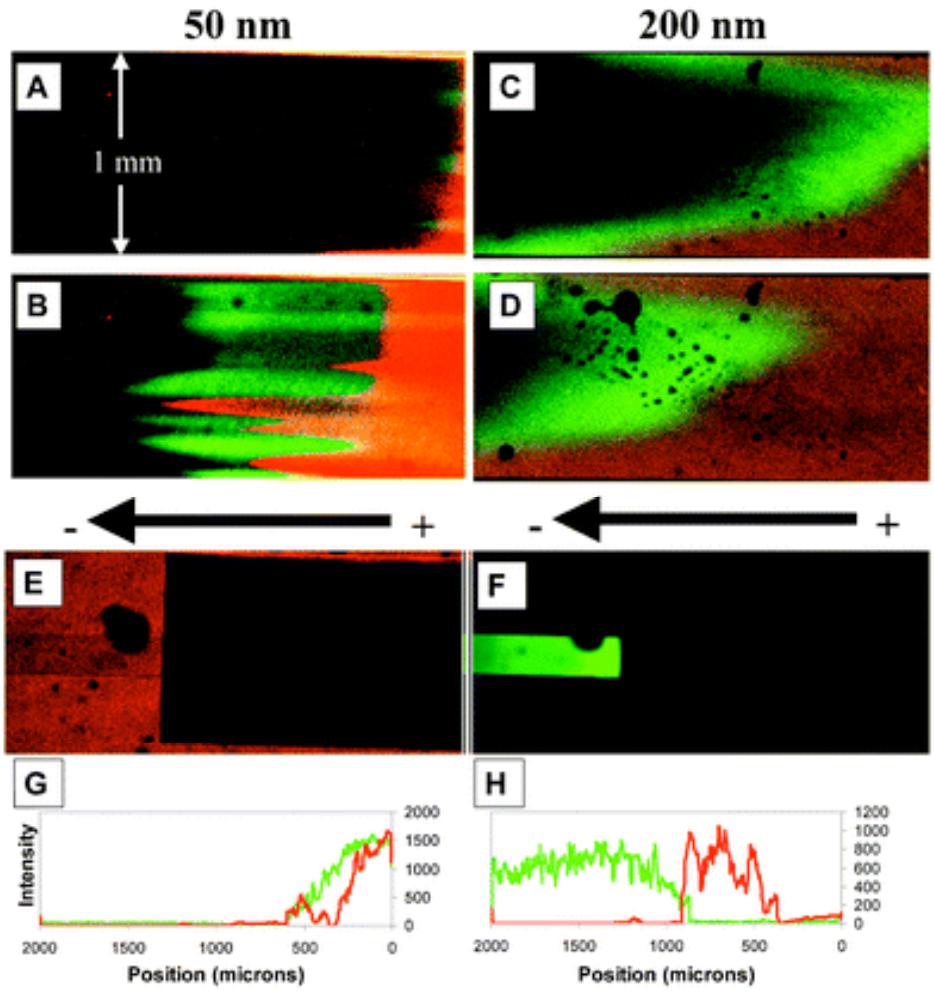

Figure 26: Sample two-color fluorescence micrographs (green = Alexa 488, red = rhodamine B) showing separation of dyes in nanochannel arrays containing channels ~50 nm wide at (A) time t=0 and (B) t=30 sec, and ~200 nm wide channels at (C) time t=0 and (D) t=25.2 sec. (E) and (F) are a micrographs of the far end of the nanochannel array near well 3 in which the red detector channel (E) and green detector channel (F) are shown separately. In the 50 nm channels at t = 600 sec the green Alexa dye has exited the nanochannels completely and is solely in the microchannel (F) while the red rhodamine B dye has not reached the far end yet (E). (G) and (H) show fluorescence intensity profiles for the two dyes in ~100 nm wide channels at (G) time t=0 sec and (H) t=290 sec. The dark splotches in the micrographs are due to defects in the Pyrex lid formed during anodic bonding. They do not affect flow in the nanochannels.

Separation of the dye fronts begins very close to the entry to the nanochannels (in all cases less than 1 mm from the entrance); the negatively charged dye (Alexa 488) had a faster velocity than the neutral dye (rhodamine B) towards the negatively biased electrode. This behavior is opposite to what is expected [48] for electrokinetic transport of the dyes in larger scale channels where electrophoresis toward the positive electrode slows the electroosmotic transport of the negatively charged species relative to the neutral one. By creating bands of dye, we were able to completely separate the two dyes within the nanochannel array. An example of this separation in 50 nm wide channels can be seen in Figure 26E and F. Here a band of Alexa dye has exited the nanochannel array and is solely in the microchannel portion of arm 3 (Figure 26F), while at the same time the rhodamine B dye has yet to reach this end of the nanochannels (Figure 26E). In Figure 26G and Figure 26H we present another example of complete dye separation, (in channels ~100 nm in width) which takes place within less than 2 mm from the nanochannel inlet, and within a few minutes. Figure 26G shows bands in the fluorescence intensity profiles of the two dyes overlapping at the entrance of the nanochannel array at time t=0, while Figure 2H shows that a band of the negatively charged Alexa dye has moved further along the length of the array than a band of the neutral rhodamine B dye at a time t = 290 sec. This separation was achieved with a relatively low electroosmotic voltage of 15 volts.

We performed control experiments with a commercial micro T-Chip (50 μm-wide channel, Micralyne Inc.) and observed that the negatively charged Alexa lags behind rhodamine B. The commercial chip was selected because the surface of its walls is SiO_2,

which is the same as the T-chip. The data that we have found in literature [52,53] as well as our own experimental measurements show that both chips have similar surface potentials. The isoelectric point of both chips is at a pH of roughly 2.6, and the surface charges change similarly with variations in buffer pH.

We observed the effects of electrical double layer overlap by changing the width of the nanochannels (~35, ~50, ~90, ~160, and ~200 nm wide) within test chips, while keeping the ionic strength constant. It is possible to achieve a qualitatively similar objective by changing the ionic strength of the buffer at a constant channel width, however the range of ionic strength of the buffer is limited due to practical restrictions. Field strengths used in our experiments ranged from 0 to 2000 V/m. Figure 27 presents a representative data set colleted for the chips with nanochannels 160 nm in width. In all cases a linear relationship (within experimental accuracy) was observed between the imposed electric field and the measured velocity of the dye front. Thus, for a single channel width, the ratios of the velocities of the two dyes are independent of the imposed electric field, which is as expected. [48] The variation in the reproducibility of the velocities of the two different dyes is due mainly to the low volumes of the dyes within the nanochannel array and our ability to precisely detect the dye fronts, however the measured ratio of the dye velocities remains highly reproducible. As the width of the channel decreased from 200 nm to 35 nm, the ratio of the velocities of the dyes (v_{Alexa}/v_{rhod}) increased from 1.5:1 to 5.8:1 (see Figure 29).

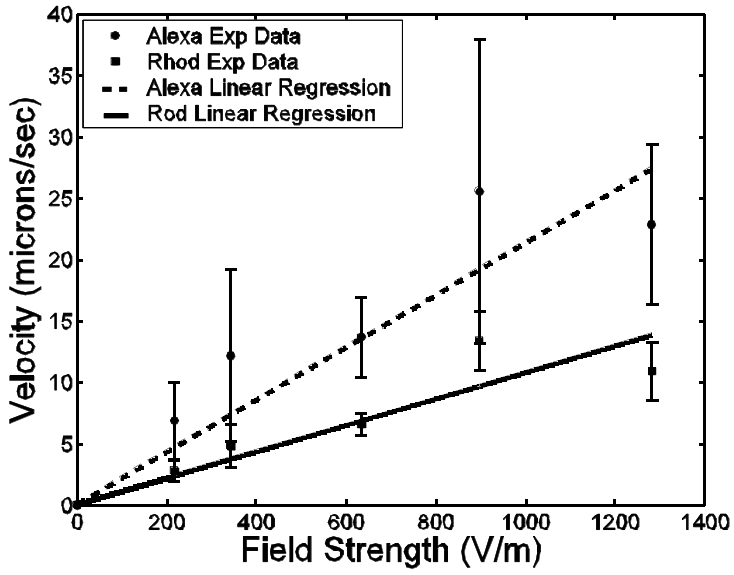

Figure 27: Plot of the experimentally observed dye front velocity vs. field strength for both Alexa 488 and rhodamine B in 160 nm nanochannels. Error bars denote the standard deviation of the measured velocity.

We considered two possible mechanisms for electrokinetic separations that occur in nanoscale channels, which are not observed in channels of larger dimensions (microchannels). The first is related to the segregation of the negatively charged Alexa dye toward the center of the nanochannels (away from the negatively charged walls) where the electroosmotic velocity is higher. The second is related to the adsorption of the neutral dye to the nanochannel walls. In the discussion below, we present a model that allows estimation of the relative contributions of these two mechanisms to the observed dye transport characteristics.

3.4 Dye Separations Theory:

At sufficiently small scales, important dimensions such as the Debye screening length ($1/\kappa$) [54] and channel width d are of the same order. In the experiments described here, the product κd varied from ~2 to 12. Described here is an approximation that allows for a theoretical treatment of the electrokinetic transport in these situations assuming a 2D flow field in channels with parallel walls and weak double layer overlap. Under these conditions, one may assume that the total electric potential between the walls of the nanochannels is simply the sum of the potentials of single walls. [48,55] With these assumptions, the dimensionless potential distribution across the width of an individual nanochannel is: [48]

$$\Psi(x) = \frac{4kT}{ze}\left[\tanh^{-1}\left(\tanh\left[\frac{ze\zeta}{4kT}\right]\exp(-\kappa x)\right)\right] + \frac{4kT}{ze}\left[\tanh^{-1}\left(\tanh\left[\frac{ze\zeta}{4kT}\right]\exp(-\kappa(d-x))\right)\right] \qquad (3.1)$$

Here z is the valency of the background electrolyte, ζ is the electrokinetic (zeta) potential of the nanochannel walls, $\kappa = \left[(2e^2z^2C_{el})/(kT\varepsilon_0\varepsilon)\right]^{1/2}$, e is the electronic charge, C_{el} is the electrolyte's number concentration, ε_0 is the dielectric permittivity of free space, ε is the relative dielectric constant of the solvent, and kT is the thermal energy. This approximation is valid for an arbitrarily high surface potential and $\kappa d \geq 2$. [54] Since the double layers from the channel walls occupy a substantial portion of the channel, the resulting electroosmotic velocity profile ($v_{eo}(x)$) is not 'plug-like' (as it is in wider microchannels), but follows the shape of the potential ($\psi(x)$). Hence, the closer to the

channel center, the faster the fluid flow. The electroosmotic and average electroosmotic velocity across a channel are given by: [48]

$$\mathrm{v}_{eo}(x) = -\frac{\varepsilon\varepsilon_o\zeta E}{d\eta}\left[1-\frac{\Psi(x)}{\zeta}\right],\ \bar{v}_{eo} = \frac{1}{d}\int_0^d \mathrm{v}_{eo}(x)dx \tag{3.2}$$

where η is the solvent viscosity. The concentration distribution of a solute across the nanochannel and the average concentration are:

$$C(x) = C_o \exp\left[-\frac{z_A e\Psi(x)}{kT}\right],\ \bar{C} = \frac{1}{d}\int_0^d C(x)dx \tag{3.3}$$

where C_0 is the solute concentration in the microchannel feeding the nanochannel array and z_A is the charge of the solute.

Separation of the two dyes within nanochannels can occur because the negatively charged walls repel the negatively charged dye, which is forced to the center of the channel (Equation 3.3). Thus, a significant portion of the charged dye occupies the region of fluid that moves fastest towards the negative electrode. The total convective flux is, by definition, concentration×fluid velocity. Since, for the negatively charged dye, both concentration and velocity have a maximum at the channel center, the effective flux of the negatively charged dye peaks sharply near the channel center. Equation 3.4 describes the concentration-weighted velocity of a dye within a nanochannel.

$$\mathrm{v}(x) = \frac{C(x)\mathrm{v}_{eo}(x)}{\bar{C}} - \mathrm{v}_{ep} \tag{3.4}$$

Here v_{ep} is the electrophoretic velocity of the negatively charged dye.

In contrast, the neutral dye is not repelled from the walls by the long-range electrostatic force, rather it distributes uniformly across the channel, and its concentration profile does not have a maximum at the center, although the fluid velocity still does. Thus, averaged across the nanochannel, it exhibits a slower velocity. In addition, molecular adsorption to the channel walls, can significantly affect separations in nanoscale channels. The charged Alexa dye is electrostatically repulsed from the nanochannel walls, preventing it from adsorbing, however a portion of the neutral rhodamine B molecules does adsorb, [56] diverting part of its flux in a direction toward the channel walls. This leads to an additional apparent "drag" for the neutral dye, reducing its net forward flux, and resulting in an overall slower velocity. For the channel geometries investigated, the wall area available for adsorption remains approximately constant as the channel width decreases; however, the total number of dye molecules in the channel decreases with the volume of the channel. Thus, the adsorption effect becomes much more significant with decreasing channel width (i.e., increasing channel surface to volume ratio).

Since rhodamine B is neutral, it is transported through the nanochannel array only by electroosmosis. Thus, by measuring the velocity in wider channels (e.g. microchannels) where we can assume that the drag due to adsorption is negligible, we can use Equation 3.2 to obtain the zeta potential, ζ. Using the velocity of rhodamine B for the 200 nm channels, we estimated $\zeta = 81$ mV, which is comparable to zeta potentials in

oxidized silicon chips reported elsewhere. [57] This value of ζ was used in the equations above to estimate the dye velocities for all other nanochannel sizes (see below).

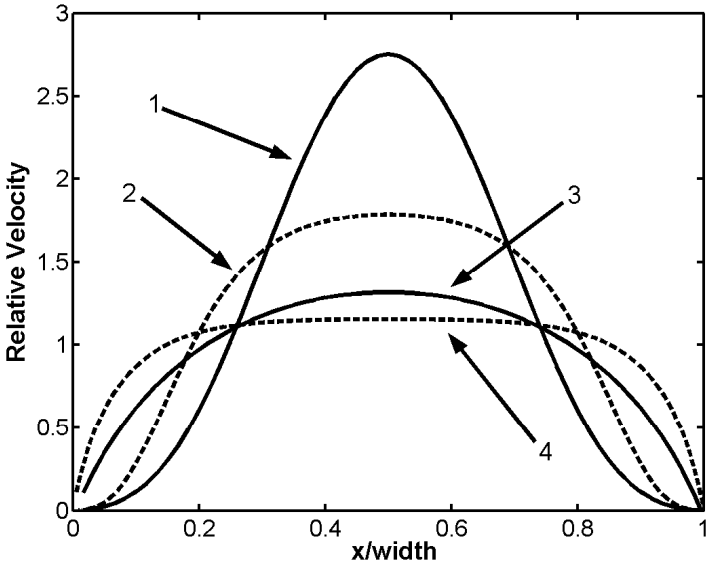

Figure 28: Dimensionless species velocity profiles due to electroosmosis for the negatively charged dye (Alexa 488) in (1) 60 nm and (2) 200 nm-wide channels and for the uncharged dye (rhodamine B) in (3) 60 nm and (4) 200 nm channels.

Figure 28 shows the normalized species velocity profiles (due to electroosmosis) of the two dyes derived from Equation 3.4 for 200 nm and 60 nm-wide nanochannels neglecting electrophoresis. Equation 3.4 predicts that the greatest difference in the maximum electrokinetic velocities will be observed at approximately 60 nm (see Figure 29); below this width ($\kappa d \sim 4$) the extent of double layer overlap reduces the potential variation across the channel, and hence the development of electroosmotic velocity profiles.

Taking into account electroosmosis, electrophoresis, and adsorption, the ratio of the maximum dye velocities may be represented by Equation 3.5.

$$\frac{\mathrm{v}_{charged}}{\mathrm{v}_{neutral}} = \frac{j_{ch\,\mathrm{arged}} - j_{electrophoresis}}{j_{neutral} - (c_{adsorption} / d)} \tag{3.5}$$

Here $j_{charged}$ and $j_{neutral}$ are the calculated maximum electroosmotic fluxes of the charged (Alexa 488) and neutral (rhodamine B) dyes respectively, and $c_{adsorption}$ is the kinetic adsorption coefficient which was obtained by fitting to the data for all nanochannel widths. The value of this coefficient is ~23 $moles/(nm \cdot \sec)$. The adsorption flux scales inversely with the surface to volume ratio ($1/d$). The electrophoretic flux, $j_{electrophoresis}$, was measured for Alexa 488 in a microchannel of known width (50 μm). [58]

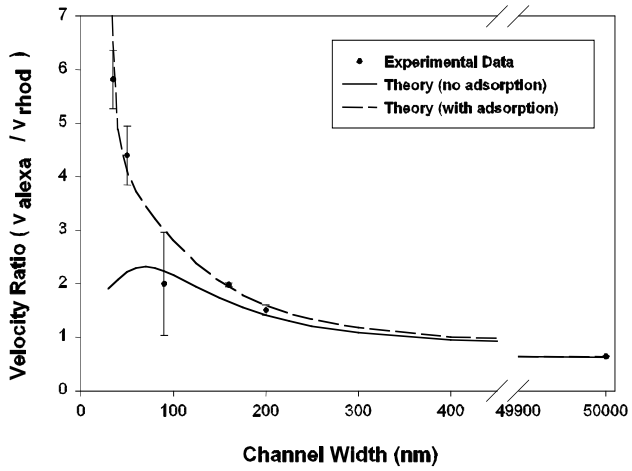

Figure 29: Experimental and theoretical ratios of velocities of dyes (v_{Alexa}/v_{rhod}) vs. width of nanochannel. The experimental ratio is the ratio of the slopes of lines obtained by least squares linear regression of dye front velocity versus applied voltage. The theoretical ratios are obtained from Equation 3.5. Error bars are typically obtained by evaluating the standard deviation for velocities obtained at five different field strengths.

A plot of the theoretical ratio of velocities with and without adsorption, from Equation 3.5, along with the experimentally measured ratios, as a function of nanochannel width, is given in Figure 29. Using this plot we estimate that below a width of ~400 nm (κd~25), the flux of the negatively charged species towards the negatively charged electrode is greater than the flux of the neutral species. Also based on Figure 29, one can see that the dominant mechanism for separation of these dyes in channels ranging from ~60 to 400 nm in width is the electrostatic segregation of the negatively charged dye towards the center of the channel where electroosmotic flux is maximum. Adsorption of the neutral dye plays a more significant role in separations in channels below ~60 nm in width (based on the differences between the curve that accounts for adsorption and the curve without adsorption and the horizontal line where the velocity ratio is equal to one).

There is good agreement between the model and our experimental observations for channel widths ranging from 35 nm to 50 μm. Similar separation of the dyes, resulting from parabolic velocity profiles, was also achieved by applying a pressure gradient to drive the fluid in the channels (data not shown).

3.5 Dye Separations Conclusions:

In conclusion, we have shown that nanoconfinement of electrokinetic transport results in well-behaved separation of dyes, which differs from that typical of larger fluidic systems and, importantly, which can be observed at much shorter distances. Spatially averaged electrokinetic transport in these nanoscale channels can effectively be observed by confocal scanning laser fluorescence microscopy. The experimental data agrees well with a continuum-based analytical model for which the ratio of dye velocities increases as channel width decreases, because of increased localization of the charged dye in the center of the channel, where the electroosmotic flow velocity is greatest, and because of adsorption of the neutral dye on the channel walls. Under the ionic strength conditions of this study, the electrokinetic model is expected to remain valid in channels wider than ~30 nm (κd~2), below which, the assumption of weak double layer overlap breaks down. Further refinement of the model will take into account the shape of the channel cross section. We have begun to quantify the effectiveness of pressure driven separations of these solutes, and to investigate other molecular species including peptides, proteins and DNA. Decreasing the nanochannel width leads to qualitatively new and counterintuitive behavior that can be exploited for molecular separations.

The separation principles described here can also be utilized to perform dye separations in other nanofluidic devices, such as the pressure driven apparatus described in the following chaper.

3.6 Dye Separations Acknowledgements:

The work presented in this section was performed as part of a large collaboration between various professionals including Dr. Michael J. O'Brien, Linnea Ista, Paul Bisong, Dr. Steven R. Brueck and Dr. Gabriel P. Lopez. We thank Dr. K. Artyushkova and Mr. R. Bradley for technical assistance, and Dr. S. Sibbett for critical reading of this manuscript. Funding for this work was provided by the NSF (NER: CTS-0304237, NIRT: CTS-0404124 IGERT: DGE-00114319) and the W.M. Keck Foundation. Additional funding for personnel salaries was provided by the ARO and the Intel Corporation. Images in this paper were generated at the University of New Mexico Cancer Research Facility.

Chapter 4: Pressure Driven Separations in Sub Micron Diameter Capillaries

4.1 Pressure Introduction

Fluid flow through microscale capillaries has been the foundation of many high performance separation techniques for many years. However separations seen in these μm in diameter capillaries are very time consuming and require high pressures or voltages to drive flow. By scaling down the diameters of these capillaries to the nanoscale, the electrical double layers originating from the charged walls of the capillaries overlap causing charged molecules to redistribute themselves in the radial direction accordingly. We can utilize the unique properties of nanoconfined fluids to achieve separations that are not possible on larger length scales. Recently the fabrication of capillaries with sub μm inner diameters has allowed for these experimental studies to be performed. Using laser scanning confocal microscopy and UV adsorption detection we demonstrate the charge-based pressure driven separation of fluorescent dyes.

As MEMS and μ-TAS technologies have advanced, characterizing fluid flow phenomena in submicron scale conduits has become an increasingly important problem [59]. There have been a substantial number of studies examining transport within capillaries caused by applying an electrical potential gradient across a capillary [60]. However, in some cases, it is not amenable to use high voltages to control transport of the molecules of interest [61]. There have been a few studies in which a pressure gradient

was used to drive transport [62,63]. However, these effects have not been experimentally studied in cases where there is a significant overlap in the double layers that arise from the capillary walls. This double layer overlap produces distinctive effects on the transport of charged molecules within the capillary. These effects are unique to nanofluidic systems and can be utilized for separations of biomolecules (nucleic acids, proteins, peptides, etc…), which often have an electrostatic charge. Separations of this manner have been demonstrated in nanochannel arrays using electroosmosis as a driving mechanism [64].

Recently in a study by Petsev [65], the electrostatic potential within a narrow cylindrical capillary has been analytically solved, and the electroosmotic velocity of an electrolytic fluid has been derived. By substituting a pressure gradient as the transport driving force, here we describe how we can use this nano-scale (in diameter) capillary to achieve pressure driven separations of charged molecules that can be done over a shorter length span than in micro-scale capillaries. Since these separations take place in a smaller conduit, they require fewer reagents, which can be important when studying molecules of a limited supply or high cost.

4.2 Pressure Experimental

4.2.1 Materials:

A commercial capillary electrophoresis (CE) instrument (P/ACE 5000 with UV detection, Beckman Coulter, Fullerton, CA) was used to provide the pressure driving the transport within the capillaries as well as detect the analytes being studied. A tank of

compressed nitrogen was used as the pressure source. The pressure separations were performed in 900 nm ID pulled fused silica capillaries (Polymicro Technologies). These capillaries were cleaved to make them a standard length of 27 cm. A 3 mm long window was made 20 cm from the inlet of the capillary by thermally removing the polyamide coating in that region. The capillary was then housed in a standard capillary electrophoresis cartridge (Beckman eCAP). The cartridge was modified to make sure the uncoated window was aligned with the UV detector window in the cartridge, and that there was a tight seal for the experiments to run correctly. A 57 cm long by 75 μm ID capillary (eCAP) was also used to do control experiments in a system where the Debye screening lengths were negligible in regards to the capillary diameter. Solutions of dyes, rhodamine B (MW = 479 Da), Alexa 488 (MW = 720 Da), Potassium Indigo (MW = 616.72 Da), and Methyl Orange (MW = 327.34 Da), were prepared in DI water, each at a concentration of 5 mg/ml. At pH 7.0, rhodamine B is neutral, methyl orange has a –1 charge, Alexa 488 has a –2 charge, and potassium indigo has a –4 charge (66). The addition of the charged dyes to the bulk solution contributes a negligible increase in the ionic strength of the system. A solution of 0.1% acetone was also prepared, which would be used as a neutral marker.

4.2.2 Method:

The capillary was conditioned by pumping Capillary Regenerator Solution A (Beckman Coulter) through the capillary at 20 psi for 30 minutes, and then rinsing with DI water for 60 minutes again at 20 psi. The analytes were injected into the capillary for

0.2 minutes at 20 psi, and then that capillary end was placed in a fresh vile of DI water for 0.2 minutes to rinse off excess dye that might contaminate the running fluid. The analytes were then pushed through the capillary for 200-250 minutes at 20-psi driving pressure. During the separation phase, both the inlet and the outlet of the capillary were kept in a vial of fresh DI water to prevent evaporation of fluid within the capillary. As each analyte passed through the UV detector, they absorbed the UV (214 nm wavelength) light, producing spikes in the output of the device. This output resembles a standard electropherogram, typically seen in electrophoretic separation experiments. The UV detector was set to take data at 5 Hz, with a sensitivity of 0.005 AU. Data was collected using P/ACE Station software. After each experimental run, pumping 0.1 M NaOH for 30 minutes at 20 psi, and rinsing with DI water for 30 minutes cleaned the capillary.

4.2.3 Visualization:

In addition to the experiments done in the P/ACE system, experiments were performed to visualize the transport within the capillaries. A 5-10 cm long segment of the capillary was cleaved and a 3 cm long window in the polyamide coating was thermally removed. The capillary was then encapsulated in PDMS to provide support as the pumping caused vibrations, which obscured images when not in PDMS. A confocal laser-scanning microscope (Zeiss Axioskop with an LSM5 scanning head) was used to capture images of fluorescent dye transport. The relatively long length of these capillaries, and

the high degree of background fluorescence of the PDMS, made it difficult to get quantitative data from these images, thus velocities and separations were measured in the commercial capillary electrophoresis device (specifically the P/ACE system).

4.3 Pressure Experimental Results

Figure 30 displays laser-induced fluorescence micrographs that demonstrate dye transport within these sub micron scale capillaries. A binary mixture of rhodamine B and Alexa 488 was introduced into a capillary filled with DI and 10% SDS (to prevent adsorption of rhodamine B) and 60-psi of pressure was applied to push the dyes through. The dyes entered the capillary as a mixture, but the front of the negatively charged Alexa passed through the viewing region well before the front of the neutral rhodamine B. The measured velocity of Alexa was 10.9 ± 0.2 μm/s, while the measured velocity for rhodamine B was 6.2 ± 0.4 μm/s.

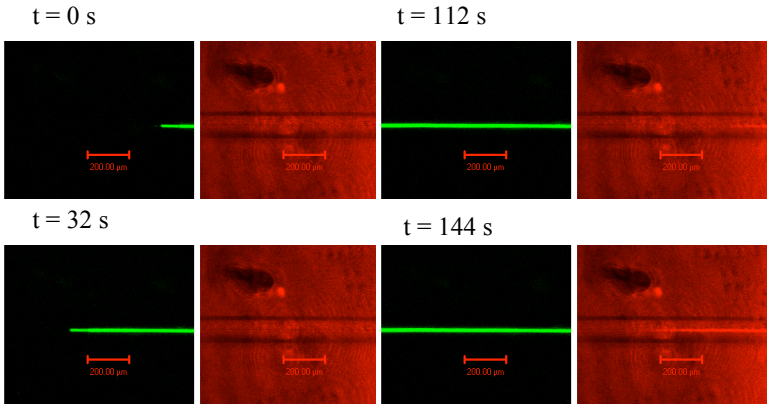

Figure 30: Sample two-color fluorescence micrographs of Alexa 488 (green) and rhodamine B (red) showing dye transport within a 900 nm ID capillary. 60 psi was applied to the right end of the capillary to induce fluid flow. The red and green detector channels were separated so that each can be seen individually, with the green detector channel on the left and red detector channel on the right.

Separations that were performed with the P/ACE 5000 system can be seen in Figure 31 and Figure 32. The capillary was initially filled with DI water before injecting the dyes into the capillary. During the separation run, DI water was pumped through the capillary at 20 psi to drive the fluid flow. After each run, the capillary was rinsed with DI water for several hours, and then conditioned with 0.1 M NaOH for 30 minutes and rinsed again with DI water for 30 minutes to prepare the capillary for future experiments. Figure 31A shows acetone traveling through the 900 nm capillary. Figure 31B shows a mixture of acetone and Potassium Indigo. A distinct peak can be seen at ~ 25 minutes, which corresponds to a velocity of 133.3 ± 15 μm/s. Figure 31C shows a mixture of Methyl Orange and Potassium Indigo traveling through the capillary. While a visible separation cannot be seen, the broad main peak (most likely due to overlapping dye peaks) occurs at a point much sooner than the acetone peak around 100 minutes, as

opposed to 148 minutes for acetone. This corresponds to a measured velocity of 22.5 ± 5 μm/s for bulk DI water and 33.33 ± 5 μm/s for the Indigo/Methyl Orange mixture.

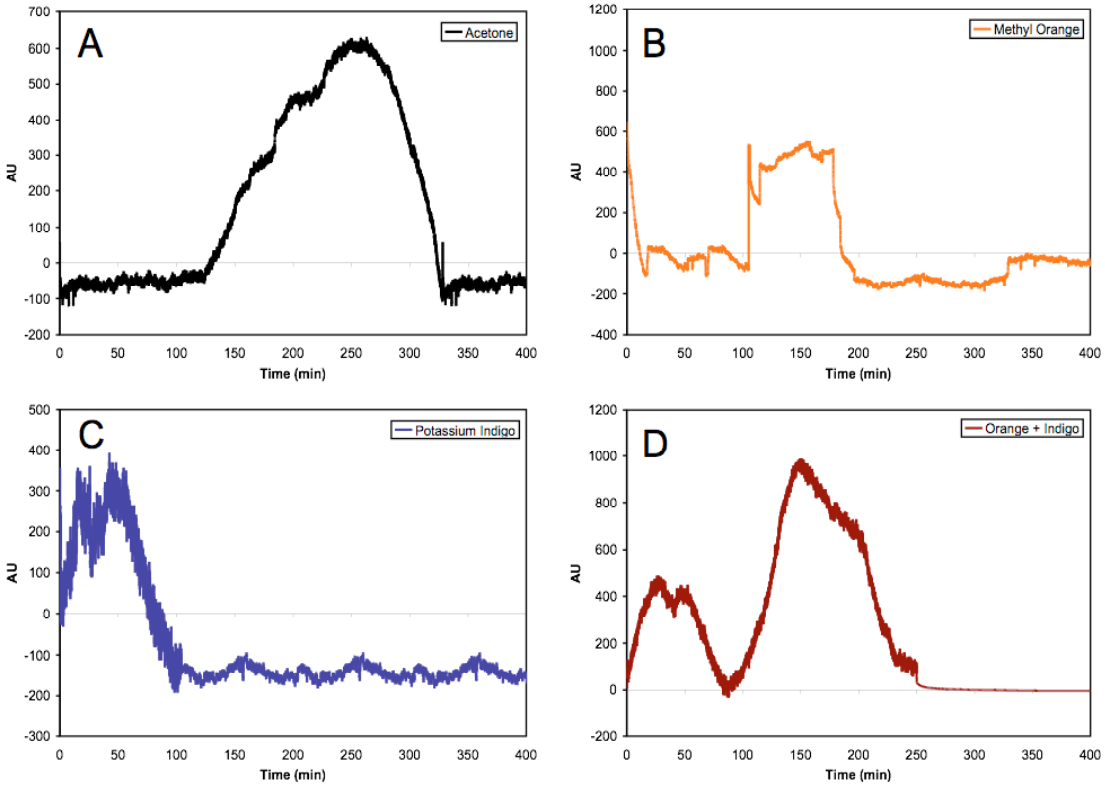

Figure 31: Dye separation adsorption traces in the 900 nm ID capillary. (A) Acetone (neutral) in DI. (B) Methyl Orange (-1 charge) in DI. (C) Potassium Indigo (-4 charge) in DI. (D) A separation of a mixture of Potassium Indigo and Methyl Orange (in this experiment it appears the detector stopped functioning at t = 250 minutes). Actual velocities are difficult to determine because the initial time of injection and actual separation run time proved troublesome to quantify reliably.

Figure 32 shows a typical result of a typical pressure driven separation experiment conducted in a 75 micron ID capillary with a 20 psi driving pressure (in this case a mixture of Methyl Orange and Potassium Indigo were injected into the capillary). As expected, there was never a case where multiple peaks, denoting a separation, were achieved.

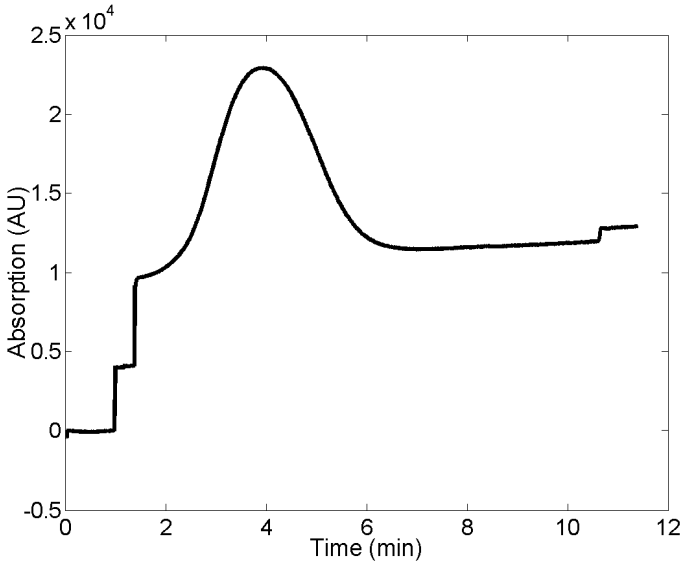

Figure 32: Dye separation electropherograms in 75 μm ID capillary. Separation step begins at t = 1.8 min. Different 'ledges' denote injection and separation steps.

4.4 Pressure Theory:

A balance of momentum and continuity gives the equation of motion for laminar fluid flow within a cylindrical capillary [67]:

$$\frac{\partial V_Z}{\partial t} = -\frac{1}{\rho}\frac{dP}{dz} + \nu\frac{1}{r}\frac{\partial}{\partial r}\left(r\frac{\partial V_Z}{\partial r}\right) \tag{4.1}$$

This can be simplified get to the Poiseuille's Law, which describes the parabolic shaped velocity profile of the fluid as a function of radial position [68]:

$$V(r) = \frac{R^2 - r^2}{4\eta}\frac{\Delta P}{L}, \qquad \overline{V} = \frac{1}{d}\int_0^d V(r)dr \tag{4.2}$$

where η is the viscosity of the fluid, $\Delta P/L$ is the pressure drop over the length of the capillary, R is the inner radius of the capillary, and r is the distance from the central axis of capillary. Equation 4.2 was solved for DI water, in a 27 cm capillary with a driving pressure of 20 psi, the result can be seen in

Figure 33.

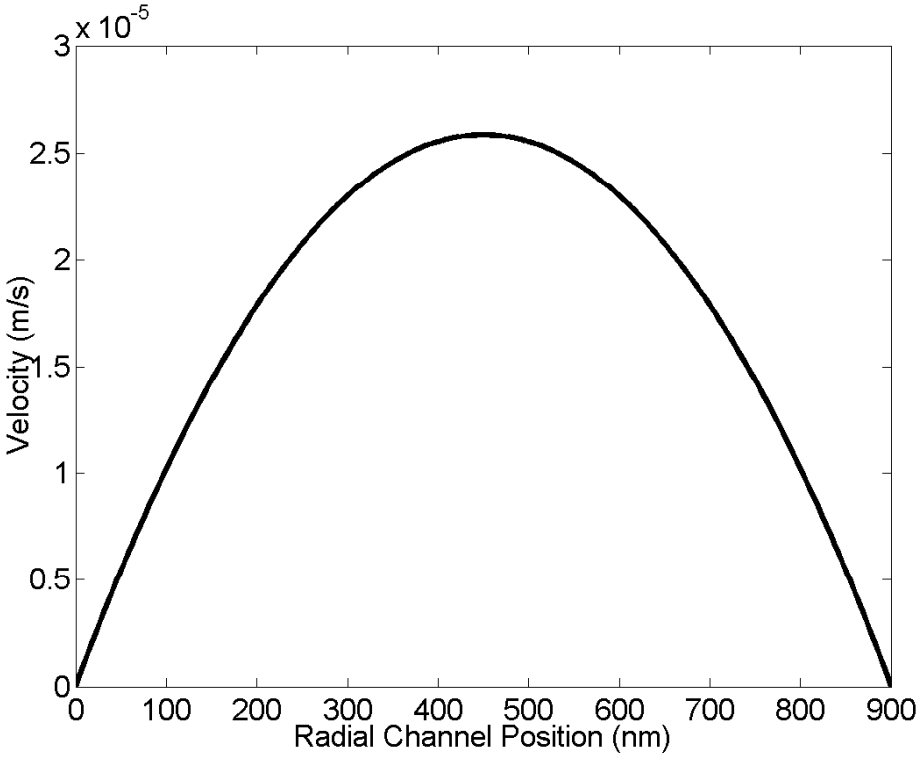

Figure 33: Fluid velocity within a 900 nm inner diameter capillary with a driving pressure of 20 psi.

Separations of charged molecules using this parabolic velocity profile occur because more negatively charged molecules will be transported within the capillary faster as they are repelled by the negatively charged walls towards the center of the capillary where fluid velocity is fastest. Less negatively charged molecules are distributed more evenly along the diameter of the capillary, thus their average velocity will be closer to that of the bulk fluid. These electrostatic interactions become more significant as the capillary diameter becomes smaller and Debye length becomes longer.

In order to determine the velocity of charged molecules of interest, their interactions with the electrostatic potential arising from the inner surface of the capillary must be accounted for. The Poisson-Boltzmann equation for a cylindrical capillary that is filled with a symmetric electrolyte is given by [69]:

$$\frac{d^2\tilde{\Psi}}{dr^2} = \frac{1}{r}\frac{d\tilde{\Psi}}{dr} = \kappa^2 \sinh(\tilde{\Psi}) \ , \ \tilde{\Psi} = \frac{ze\Psi}{kT} \tag{4.3}$$

where ψ is the electrostatic potential, r is the radius, z is the valence of the background electrolyte, e is the charged of an electron, and kT is the thermal energy. Equation 3 was solved numerically and the electrostatic potential profile in a 900 nm silica capillary filled with DI water ($\kappa R \approx 1$) can be seen in Figure 34 below. The Stern Layer was neglected, meaning $\psi = \zeta = -104$ mV (64) at the walls, and continuity was assumed meaning $\nabla\psi = 0$ at the center of the capillary.

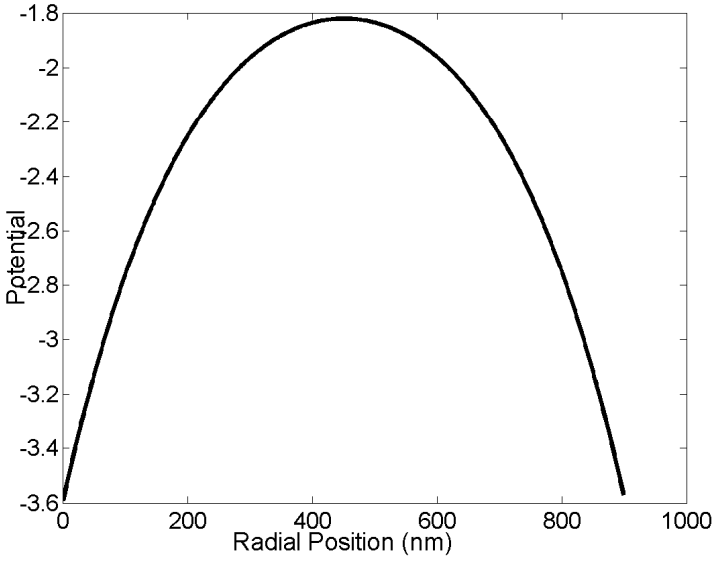

Figure 34: Electrostatic potential (non-dimensionalized by e/kT) within a 900 nm ID silica capillary filled with DI water.

The radial concentration distribution and average concentration of a charged molecule within the capillary is given by:

$$C(r) = \exp\left[-\frac{z_A e\Psi(r)}{kT}\right], \qquad \overline{C} = \frac{1}{d}\int_0^d C(r)dr \tag{4.4}$$

where z_A is the charge of a specific analyte. For negatively charged analytes, both the concentration and fluid velocity profiles have a maximum at the center of the capillary. This means that the effective flux for charged molecules should have a sharp peak at the center as well. Equation 4.5, describes the normalized concentration-weighted analyte velocity within the capillary.

$$v_{analyte}(r) = \frac{C(r) * V(r)}{\overline{C} * \overline{V}} \tag{4.5}$$

Figure 6 below shows the normalized pressure driven velocities within a 900 nm silica capillary filled with DI water for Potassium Indigo (-4 charge), Methyl Orange (-1 charge), and for the bulk fluid.

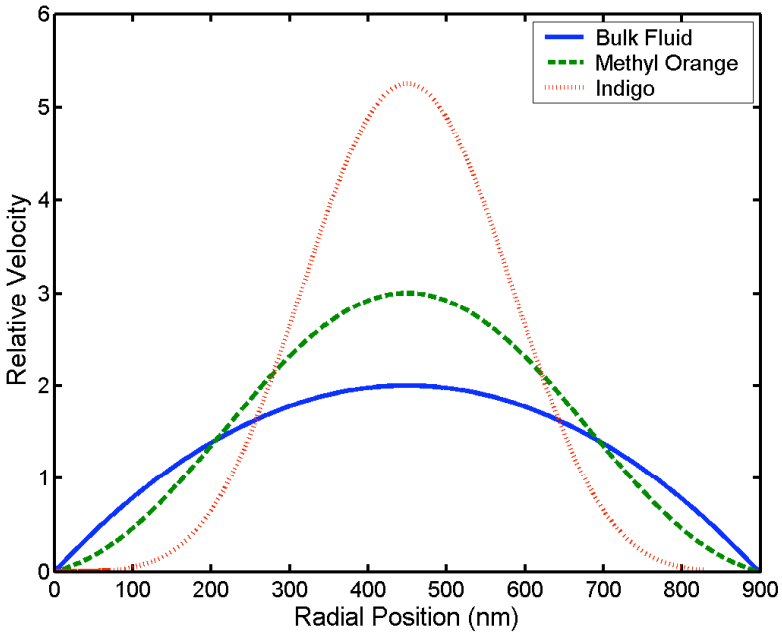

Figure 35: Normalized concentration weighted velocities for Potassium Indigo, Methyl Orange, and bulk DI water (experimentally measured with 0.1% Acetone) within a 900 nm ID silica capillary filled with DI water.

From this model, the average velocity of the fluid is calculated to be 17.2 μm/s, which is in relatively good agreement with the measured velocity from the UV absorption experiments.

4.5 Pressure Conclusion

In conclusion, we have demonstrated that nanoconfinement of charged molecules can be utilized to achieve separations using pressure to drive fluidic transport within capillaries that have sub micron inner diameters. Transport within these small conduits can be visualized using laser scanning confocal microscopy, and separations can be measured using UV absorption from commercial capillary electrophoresis device. The experimental data agrees qualitatively well with the theoretical model that accounts for the significant double layer overlap ($\kappa R \approx 1$ for DI water), and the cylindrical geometry in this system. The more negatively charged dyes travel through the capillary to the detector more rapidly than the less charged dyes, with velocities that are comparable to the theoretical model presented here. However, the wide electropherogram like adsorption data prevents us from making accurate velocity predictions. This study has proven the same separation principles that were presented in the on-chip dye separation section can be utilized to perform similar separations in other nanofluidic devices.

Investigations into the separations of biological molecules, analyzing the effects of different ionic strength running buffer, and performing studies to quantify the deviation of pressure driven bulk fluid velocity from classical Poiseuille flow due to the electroviscous effects that become significant on this scale should be the next steps in characterizing this pressure driven nanofluidic separation system.

The work done in this study, especially in the characterization of the addition of surfactants, and in the cleaning and preparation of the capillaries proved to be of great help in following studies in performing separations of biological materials. This work is discussed further in the following chapter.

Chapter 5: Electrokinetic Separations of Proteins in Chip Based Nanofluidic Channels

5.1 Protein Introduction:

Recently the extrication and purification of important biomolecules including proteins have been a topic of great interest. Methods for separation of proteins can be generally grouped into two categories, preparative or analytical. The goal in performing preparative purifications is to obtain purified proteins which can be later be used in other areas. These include the isolation of commercial proteins such as enzymes, nutritional proteins, or particular biopharmaceuticals (i.e. insulin). On the other hand, analytical purification is used to produce a relatively small amount of a protein for a variety of analytical purposes, including identification, quantification, and studies of the protein's structure and function.

Polyacrylamide gel electrophoresis (PAGE) has been the standard technique for performing many of these types of separations. [70] In spite of its success, this technique has several limitations and drawbacks including the amount of gel preparation time, the repeatability in gel fabrication, the amount of reagent needed to perform separations, the high voltages needed, and the difficulties involved when trying to integrate the results of separations with quantification tools (such as mass spectroscopy). These inherent

limitations that transpire when using PAGE to perform separations has lead to an increase in the study of microfluidic, lab-on-a-chip (LOC) type devices. [71,72,73] Recently, there have been several technological innovations that have scaled down these microfluidic systems into the nanofluidic regime. [74] These new nanofluidic devices promise increased speed and resolution of separation, reduced cost and sample sizes, and enhanced flow controllability over their microfluidic counterparts. [75, 76, 77, 78]

Numerous studies using nanofluidic devices to perform protein separations have been made because of these potential benefits. [79, 80, 81, 82, 83, 84] However, these studies have revealed many difficulties in working with proteins, especially in silicon-based chip devices. As these systems get smaller, fouling of the channels becomes more of an issue, causing chips to have short working lifetimes, if they work at all.

This section presents a study that addresses of the many issues that have been observed in previous and concurrent protein separation studies, and develops methodologies that can be used when trying to separate proteins in chip-based nanofluidic systems. This study also explores the different mechanisms that can be utilized to perform separations in nanofluidic systems, including protein valence, chromatographic exclusion, and hydrodynamic chromatography effects. A novel model to describe size based hydrodynamic chromatography in nanofluidic systems is developed here.

5.2 Protein Separations, Experimental Section:

5.2.1 Apparatus

Experimental observations were made using the T-Chip nanofluidic system used previously to explore transport and charge based separation of dyes. [78] In this configuration, an array of about 2000 nanofluidic channels, of various specific cross sections and 1 cm long, is integrated in a cross shaped layout with microfluidic channels that allow for the introduction of analytes into the nanofluidic array. Large reservoirs are placed at the ends of the microfluidic channels where buffer is held, analytes are injected, and the electrical potential that drives transport can be applied. A micrograph of the test chip can be seen in Figure 36.

Figure 36: Photograph of a standard T-Chip type device that is used in experimental efforts. Note the nanoport reservoirs are bonded to the surface of the chip to allow for sample injection. Since this is a used chip, the left and right wells are discolored from the proteins/dyes that have collected in the respective reservoirs.

5.2.2 Data Collection:

Experimental observations were recorded using a LSM 510 laser scanning confocal microscope (Zeiss Inc.). Fluorescence intensity data were colleted from micrographs harvested from the microscope and velocities were extrapolated via a Matlab routine that was able to quantify the change in position of the fluorescent front of the proteins being observed.

5.2.3 Proteins:

We selected several proteins of interest in our study based on their size differences, their ability to be fluorescently tagged with unique fluorophores, their valence, their shape and stability, and their availability. The proteins selected and their molecular structure [85] can be seen in Figure 37. A fifth protein, neutravidin (not

shown), was also used because it has a valence of zero in the pH ranges we studied. Neutravidin is a modified avidin protein, which has similar size and weight properties as typical avidin [86].

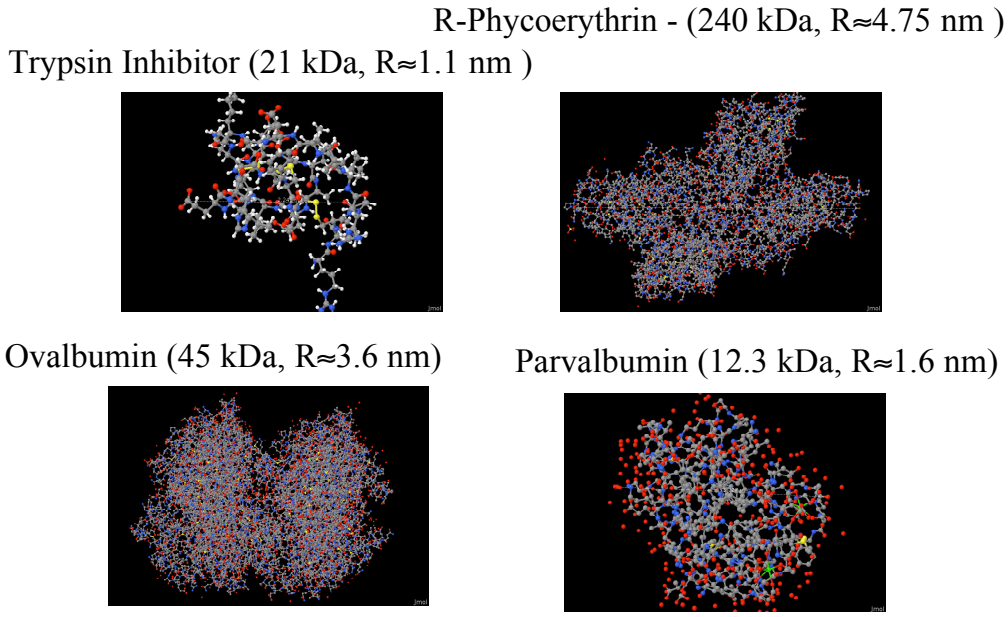

Figure 37: Molecular structures, weights and radii of proteins used in this study. Trypsin inhibitor (-10.9 as derived by its structure by the protein calculator) and parvalbumin were labeled with Alexa 488 florescent dye (green), while ovalbumin was labeled with Alexa 532 (red florescent dye), and R-Phycoerythrin (-8.9 as derived by its structure by the protein calculator) is naturally fluorescent red.

5.2.4 Surfactant Issues:

As in previous studies, [78] the T-Chip was filled with a standard Tris-Glycine electrophoresis buffer that was diluted 100x (at this level of concentration, the ionic strength of the buffer was decreased and the electrostatic double layer length increased).

Our experimental efforts focus on two main areas, systems without surfactant added, and systems with surfactant added. Surfactants are wetting agents that when added to a solution, such as buffer, lowers the surface tension of a liquid. This, in turn, prevents the adsorption of the proteins to the walls of our chip. This protein adsorption has been a major obstacle in many experimental efforts to separate proteins in micro- and especially nanofluidic devices because of the high surface to volume ratio.

In our study, the experimental efforts that did not use surfactants produced sieve like separations, in which certain molecules were excluded from the nanochannel array. In experiments where surfactant was employed, we added 8.04×10E-5 M [87] of the nonionic surfactant Tween 20, or 0.0082 M [88] of the anionic surfactant Sodium Dodecyl Sulfate (SDS) to the running buffer. This amount corresponds to the critical micelle concentration of each surfactant. Encapsulating the proteins in micelles was important to limit the amount of adsorption. We focused more on the use of the nonionic Tween 20 because it acts as an excipient, and does not change the ionic strength of the buffer used, thus does not reduce the length of the double-layer, allowing us to still be able to take advantage of its benefits for separations [89].

In the experiments where surfactants were introduced into the buffers, we used chips that were not etched as deep as was done in previous studies. By using shallower channels, specifically the microfluidic arms of the T-Chip, we were able to reduce the amount of bubble formation, which causes a breakdown in the electrical continuity within the nanofluidic channels and results in irreproducible data. An example separation in

traditional T-Chips with deeper microchannels demonstrate the bubble formation can be seen in Figure 38, where a negatively charged protein (trypsin inhibitor - green) is excluded from the nanochannel array, while a neutral protein is allowed in (neutravidin – red).

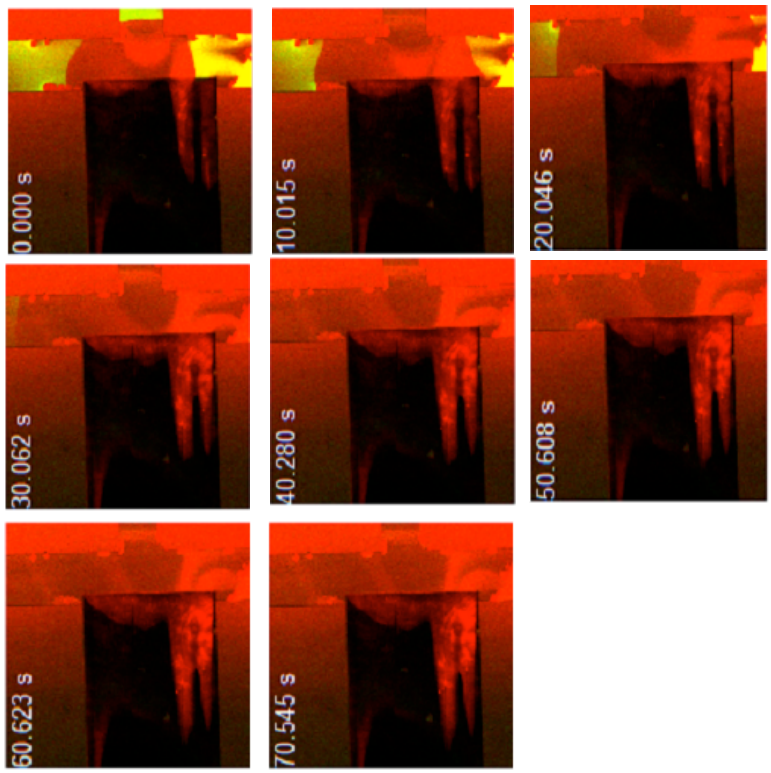

Figure 38: Typical bubble formation in separation experiment with a nanochannel width of 100 nm. The proteins used were trypsin inhibitor and neutravidin. This resulted in a separation in which the proteins moved in opposite directions once the bubble formation began. The results of this experiment were irreproducible.

Bubble formation was prevalent in the microchannel section of the chips in every experimental effort until we implemented the new chip design with nano-deep microchannels. A scanning electron microscope micrograph of a nanochannel grating on a chip with more shallow channels can be seen in Figure 39. The new depth of the microchannels was approximately 400 nm, which is at the crossover point between micro- and nanofluidic regimes for the ionic strengths used in these experiments [64]. However, separations within the microchannels were not observed.

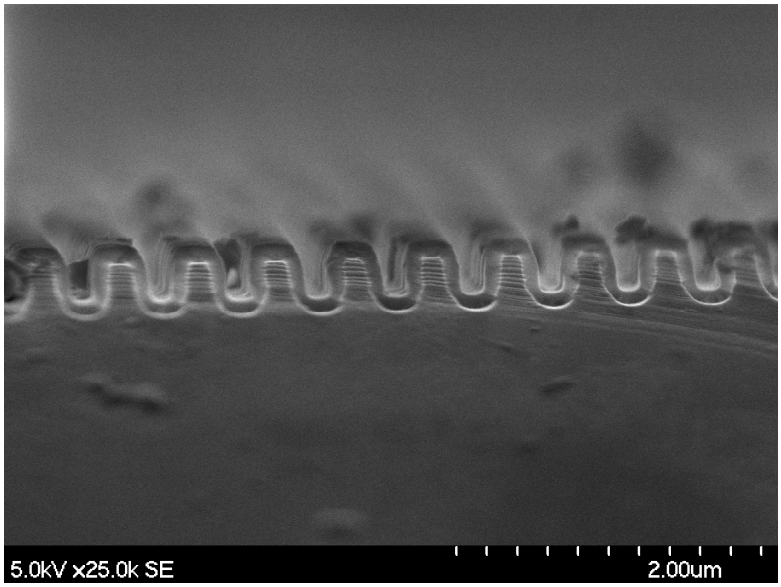

Figure 39: SEM of nanochannel grating with shorter etch time resulting in shallower channels.

Gratings with cross sections similar to those seen in previous studies were also used for separation studies in which no surfactant was added to the solution. In these chips, fouling, due to the adsorption of proteins at the channel walls, was a major concert, and severely limited the useful lifetime of the chip. Normally a chip can be used for several

experiments; the polarity of the driving potential can be reversed, the chips can be cleaned, and the analytes being observed can be cleared from the interior of the chip. However, in these experiments involving proteins, the chips can only be cleared 2-3 times before the flow becomes unobservable.

5.2.5 Separations

- 5.2.5.1 Sieving like separations

As mentioned previously, adsorption of analytes is a significant factor in nanofluidic systems. Because of the dimensions of the channels, there are smaller volumes of analytes being transported, so a greater fraction of the total mass of analyte in these channels can be adsorbed.

Certain molecules have greater affinity for adsorption, especially in our silica based fluidic systems. This provides us with a mechanism for separation. Sieving devises have been explored previously [90], and have demonstrated separations in smaller nanofluidic systems, but have been limited to entropic trapping type of devices. In our device we demonstrate sieving like separations with only a single micro- nano-interface.

Figure 40 demonstrates a typical exclusion separation experiment seen in our nanofluidic T-Chip device, here with an array of 35 nm wide channels. Here the chip was filled with the standard Tris-Glycine running buffer. A binary mixture of 5mg/ml of

Trypsin Inhibitor and Neutravidin was added to the far right (East) reservoir and moved via electroosmosis (East = -60 V, the rest set to ground) through the microchannel towards the nanochannel section. The mixture did not separate in this channel. When the mixture reached the nanochannel array the polarity of the reservoir electrodes were switched to drive the mixture into the nanochannels (East remained at -60V, North set to -60, West and South remained grounded). Here we observed that trypsin inhibitor entered the nanochannel area, while the Neutravidin remained solely in the microchannel area and did not enter the nanochannels. Trypsin inhibitor was expected to enter more easily because it is a smaller protein with low adsorption characteristics [91], while avidin is commonly used as a way to functionalize silicon based microfluidic devices in part because of its high affinity for adsorption to silica walls (it can then be used to bind to biotin and capture biotin labeled proteins; this is not a property utilized here [92]). The polarity of the driving electrodes was reversed and the proteins were cleared as much as possible from the nanochannel area, and the experiment was attempted several more times with up to a 150 Volt potential difference. Each time the Trypsin Inhibitor entered the nanochannel array, while the Neutravidin remained only in the microchannel section. A plug of pure Trypsin Inhibitor could reach the South (bottom) microchannel at the end of the nanochannel array before the nanochannel section became too fouled to allow any more protein though.

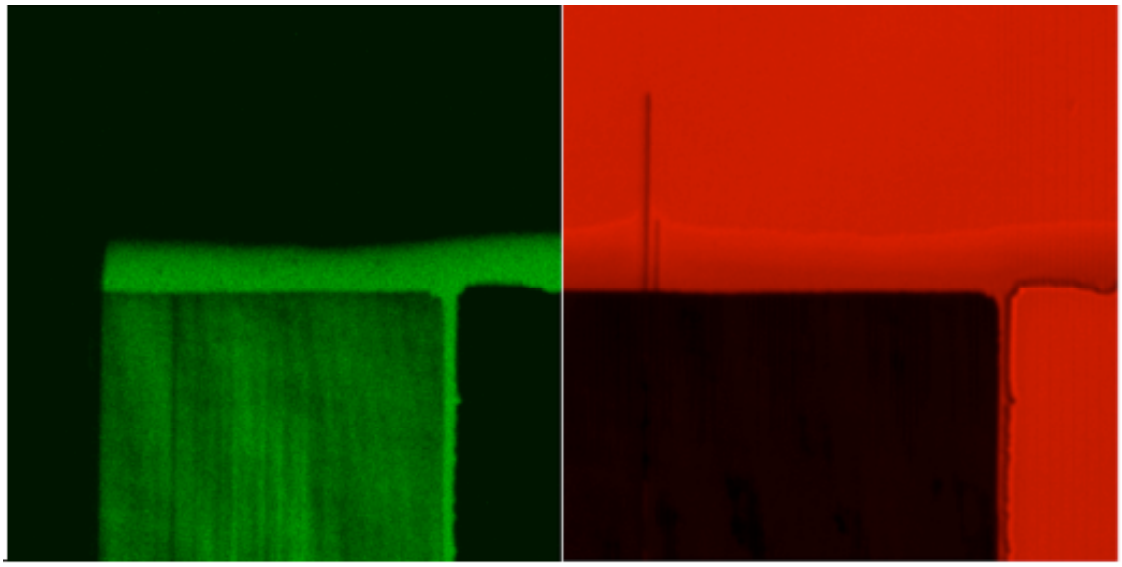

Figure 40: 35 nm channels, Trypsin Inhibitor and Neutravidin mixture at the entrance of the nanochannel array (North end or T end), demonstrating exclusion separation/purification of mixture.

Figure 41 demonstrates another example of an exclusion-based separation. Here a mixture of trypsin inhibitor and ovalbumin was introduced into the T-Chip. The mixture was electroosmotically transported through the microchannel as before and again the polarity was set to drive the mixture into the nanochannel array (here with 100 nm wide channels). Again only the trypsin inhibitor was able to enter the nanochannel array, while the ovalbumin remained only in the microchannel section. Here, because of the larger volume of the nanochannels, higher amounts of pure trypsin inhibitor reached the South end of the array.

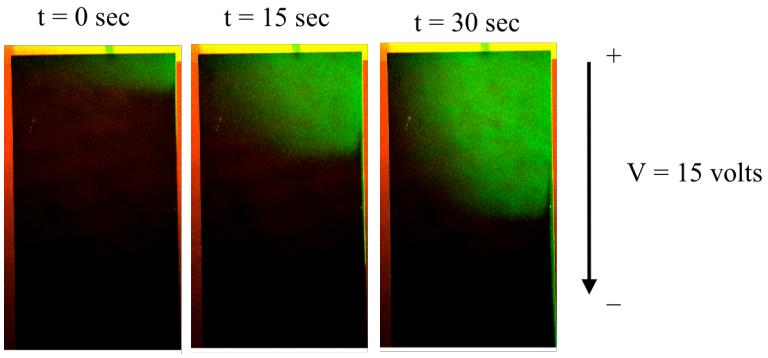

Figure 41: Micrograph of proteins in the North end of the nanochannel array in a 100 nm wide channel T-Chip with Trypsin Inhibitor and Ovalbumin demonstrating the exclusion of Ovalbumin from the nanochannel array.

While nanofluidic sieving has proven to be an effective mechanism to perform separations and purifications of proteins with different sizes and different affinities to adsorb to the channel walls, sieving has its limitations. This mechanism is only able to separate a binary mixture with proteins being able to either enter or not enter a nanochannel array. In more complex chip configurations this could be addressed by having multiple nanochannel sections, each with a unique width and able to exclude specific proteins. This leads to the other concern, the fouling of the chips as more proteins adsorb to the walls. This adsorption feature limits the resulting volume of proteins that we can extract from the chip. Efforts to reduce protein adsorption by adding surfactant to the buffer within the chip, also negates the exclusion characteristics of the chip. After adding surfactants to the buffer (at around the critical micelle concentration), proteins, that could not enter the nanochannel array before, are able to enter. Thus we must explore further mechanisms for separations.

- 5.2.5.2 Hydrodynamic Chromatography (HC):

The mechanism that we choose to explore here in this study is based on hydrodynamic chromatographic effects. These effects are typically seen in bead packed microfluidic systems, in which larger molecules exhibit faster velocities due to the fact that they cannot get closer to the walls than their hydrodynamic radius (thus they are segregated in the areas of flow that are faster. The theory behind this mechanism is explored further in the theory section.

A set of experiments was performed in the Micralyne type chip (Micralyne Inc. - 50 μm wide channels) to determine the necessary concentration of surfactant needed to reduce adsorption. Based on experimental observations, see Figure 42, the proteins must be in a buffer with a surfactant concentration high enough to encapsulate the protein molecules by surfactant micelles (at the CMC) in order for them to overcome the adsorption effects and enter the nanochannel array. There seems to be good agreement with the observed the adsorption seen in a microfluidic device and that observed in the T-Chip, that is when any adsorption was observed in the Micralyne chip (Figure 42a), no protein could enter the nanochannel array. When there was no noticeable adsorption in the Micralyne chip, see Figure 42b, there was sufficient amount of surfactant added to the buffer to allow these proteins into the nanochannel array. This concentration of added surfactant happened to coincide with the critical micelle concentration of the surfactant of interest (here Tween 20 is shown, but similar micrographs demonstrate similar effects with SDS).

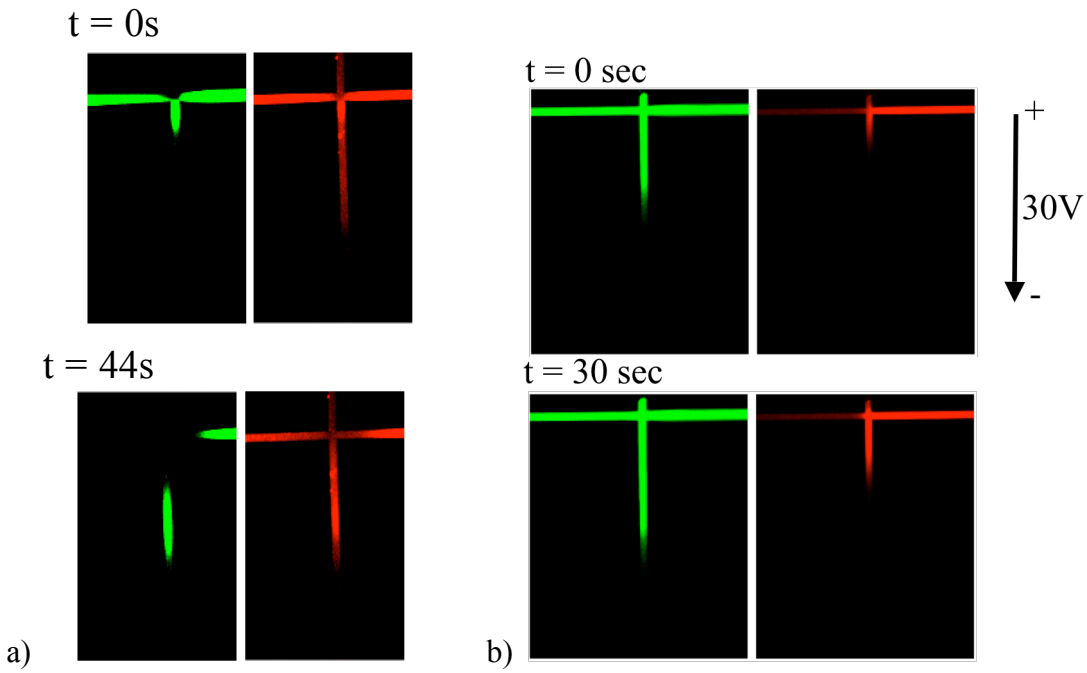

Figure 42: Micrograph of R-Phycoerythrin (red) and Trypsin Inhibitor (green) mixture within Micralyne chip a) with Tween 20 at 0.1% - below the CMC, and b) after the introduction of Tween 20 at the CMC (0.5%). The red and green channels are separated for clarity.

Because the proteins must be encapsulated in surfactant micelles to enter the nanochannel array, it is assumed that they no longer possess significantly different valences. No differences in velocity can be observed in the Micralyne chips. The different charge dye front positions seen in Figure 42 are attributed to the proteins entering the chip in slightly different times (perhaps due to differential affinities to entering the microfluidic arm of the T-Chip, since the differential is seen in that region of the chip as well). Both proteins exhibit velocities that are not statistically different from each other, indicating that the electrophoretic mobilities and thus the valences of each protein are similar.

We hoped that introducing these proteins into nanofluidic channels would allow us to utilize the unique velocity distribution seen in nanoscale devices to achieve separations. Initial experiments focused on the addition of the ionic surfactant sodium dodecyl sulfate (SDS) to the running buffer. SDS was used because it was a more effective surfactant eliminating observable adsorption in the Micralyne chips. In experiments with Tween 20, adsorption was still observed, although highly limited. However, the addition of SDS increased the ionic strength of the buffer, and lowered the magnitude of the double layer length. Figure 43 demonstrates a typical experiment with SDS at the CMC added to the buffer. A mixture of ovalbumin and parvalbumin were introduced into an 85 nm wide nanochannel array. However, once inside the nanochannels, the proteins exhibited statistically indistinguishable velocities and no observable separations.

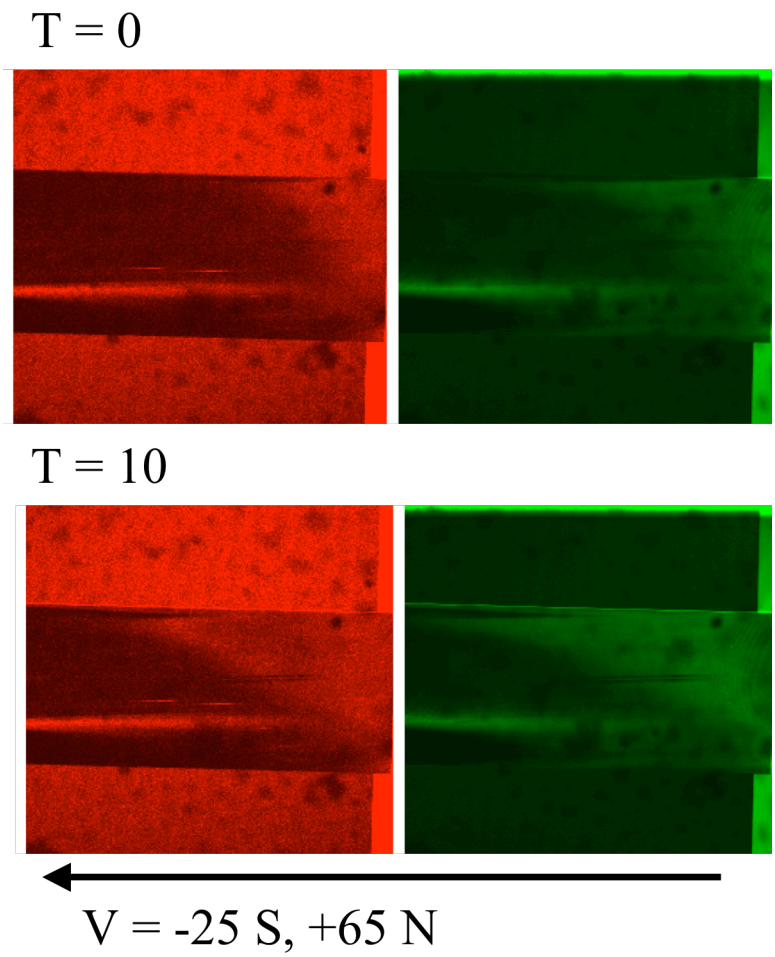

Figure 43: Micrograph of Ovalbumin (red) - Parvalbumin (green) mixture traveling through array of 85 nm wide nanochannels. Here SDS is added to the buffer allowing both proteins to enter the nanochannel array. No separation is observed.

Experimental efforts were switched to focus on the use of the nonionic Tween 20 surfactant. Again, surfactant was added to the running buffer at the CMC (here 0.5%), and a mixture of proteins was introduced into the nanochannel array. Because adsorption was more of a factor with Tween 20 than with SDS, more stable proteins were used (here R-Phycoerythrin and trypsin inhibitor – these proteins exhibited lower adsorption characteristics in the Micralyne chip). With this chip, buffer, protein, surfactant system

we were able to observe separations of these proteins within the nanochannel array. Figure 44 demonstrates a typical separation seen in 100 nm wide nanochannels. The larger protein, R-Phycoerythrin exhibits faster transport through the array (R-Phycoerythrin has a radius approximately 4x bigger than trypsin inhibitor). Both proteins are able to be transported through the array fully, and can reach the South microchannel at the end of the nanochannel array. Here the ratio in velocities R-Phycoerythrin: Trypsin Inhibitor is about 2.2:1.

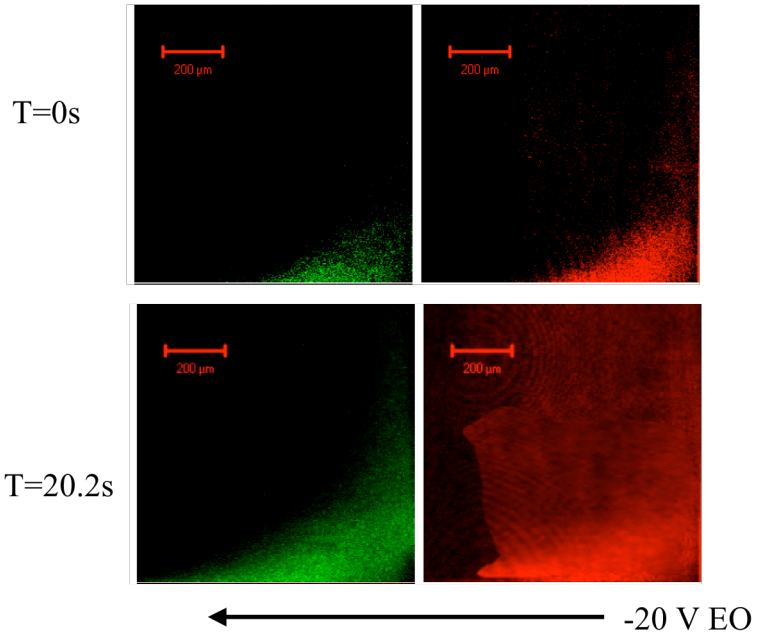

Figure 44: Separation of Trypsin Inhibitor (green) and R-Phycoerythrin (red) protein mixture in 100 nm wide nanochannels with the addition of 0.5% Tween-20 nonionic surfactant.

Similar experiments were run using smaller nanochannels (~35 nm wide). Again with the addition of Tween 20 at the CMC, both proteins were allowed to enter the nanochannel

array, and an observable difference in velocities could be observed. However the ratio of velocities is about 1.8:1. The overall observed velocities were also about half of that observed in 100 nm wide channels (see Figure 46), this is as expected because the electrostatic potential is no longer fully developed in these narrower channels, and the electroosmotic velocity is correlated to this electrostatic potential.

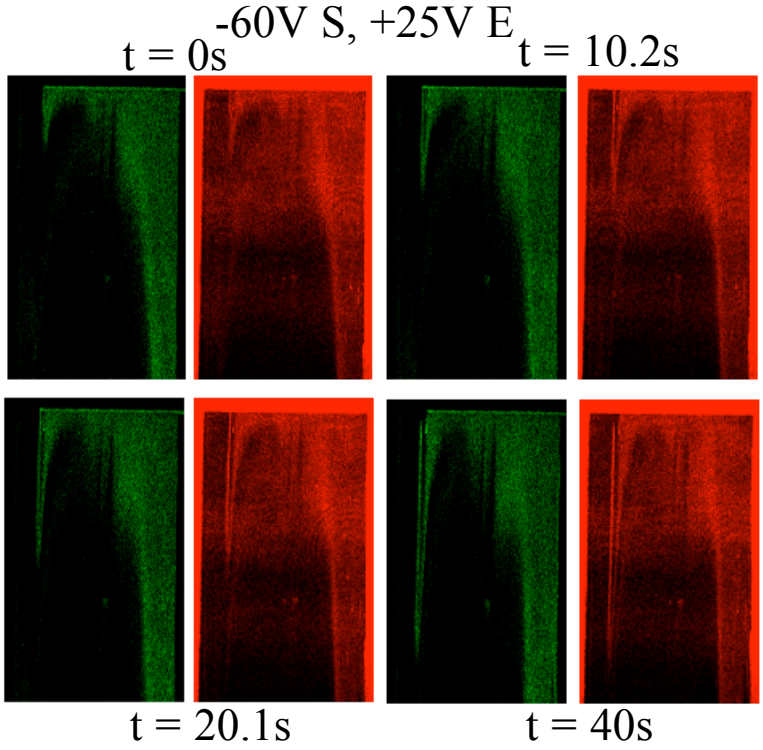

Figure 45: Micrograph demonstrating separation of R-Phycoerythrin – Trypsin Inhibitor mixture in 35 nm wide channels with the addition of 0.5% Tween 20. Separation is still observed, but not as prominent as in 100 nm channels (as explained in the theory section).

Protein front velocities were calculated in a similar manner as done in previous studies. [78] Figure 46 demonstrates typical experimental velocity data obtained. A more in depth velocity plot is shown at the end of the theory section.

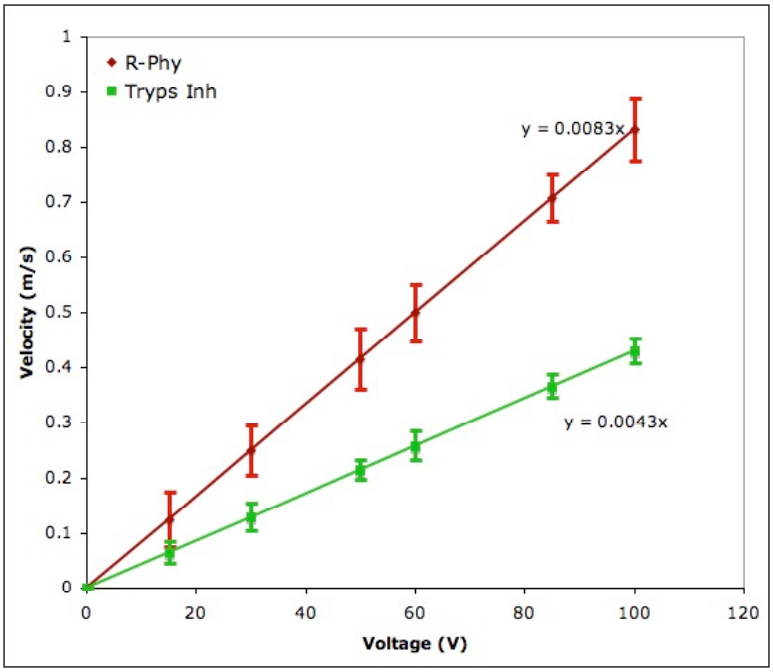

Figure 46: Sample velocity data of Trypsin Inhibitor transport in T-Chip with 100 nm wide nanochannels.

5.3 Protein Theory:

As mentioned earlier, several mechanisms can be exploited to achieve biomolecular separations in nanofluidic devices. These methods including chromatography [93], exclusion/sieving [94], and molecular valence [78], have basic

analytical models that have been described in the given references. Molecular valence based models predict that the degree of velocity difference between two molecules due to charge based exclusion from channel walls is relatively small, as can be seen in Figure 47. Separations can be achieved, but require longer path lengths, and/or large differences in molecular valence. Furthermore, separations were observed in our T-Chip system that do not agree with what is predicted by this model, thus we wanted to explore different mechanisms for feasible separations.

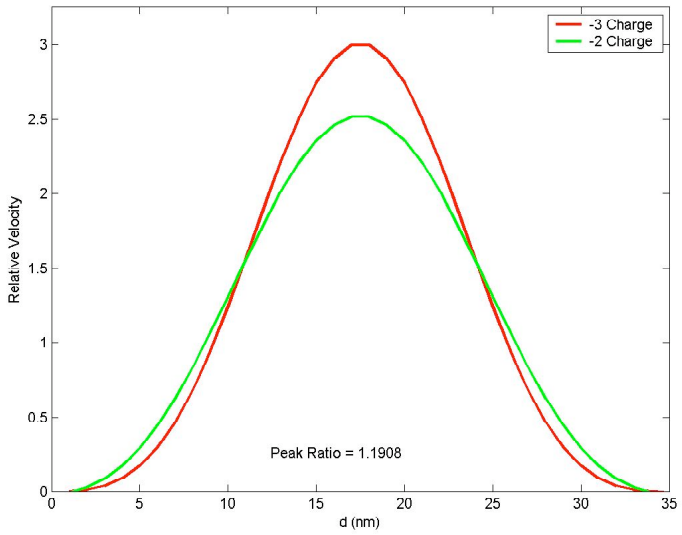

Figure 47: Relative velocity of two charged molecules (valences of -3 and -2), in 35 nm wide channels, using molecular valence model developed by Garcia *et. al.*

In this manuscript, we describe a novel separation approach that has recently been gaining interest in micro- and nanofluidic systems, known as hydrodynamic chromatography. This is made possible because when a particle is transported in a porous medium, similar to our array of nanofluidic channels, the particle's center of mass is

excluded from the slower velocity regions near the channel walls because the particle can only be as close to the wall as it's radius. Thus the average velocity of the particle is faster than the velocity of the fluid. Correspondingly, larger particles are excluded from the lower velocity regions more than smaller particles, thus larger particles possess faster velocities. A schematic of this mechanism can be seen in Figure 48.

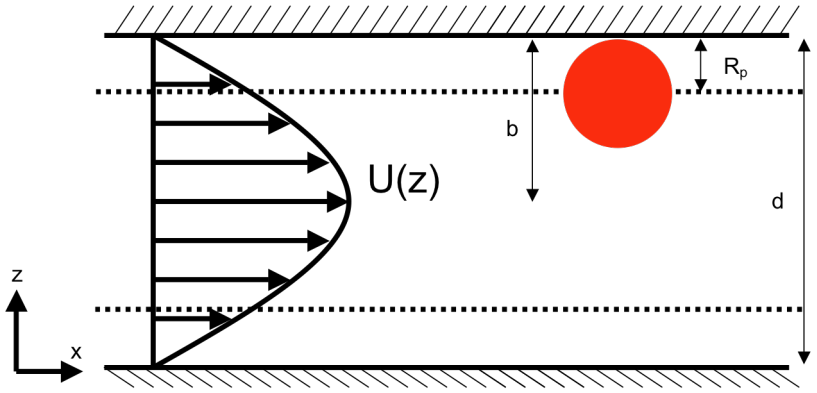

Figure 48: 2D Schematic diagram of hydrodynamic chromatography in a nanochannel.

This concept has been described in microfluidic devices as a method for achieving separation [95, 96, 97], The basic concept behind this as a separation mechanism is followed here and expanded upon to explore nanofluidic transport. These approaches have yet to be fully investigated in nanofluidic, parallel-walled, channel based devices like we have in our T-Chip. Most of these studies have focused on pressure driven methods of inducing flow within these separation devices. This was necessary because that method of flow induction provides the needed velocity distribution necessary for

separations to occur. However, because of the amount of electrostatic potential overlap seen in our nanochannels, we can produce a sufficient velocity gradient using electrokinetic means of inducing fluid flow.

Our model assumes that the channels are planar with a constant width. This is the same treatment we used to describe the potential in our higher aspect ratio channels [62] and what others have assumed in low aspect ratio channels [6]. Because of the low Reynolds number seen in nanofluidic systems, the fluid flow is assumed to be laminar, such that the bulk buffer velocity only varies in the z direction, and can be expressed as shown in Equation 5.1.

$$u(z) = \frac{-\varepsilon\varepsilon_0 E\zeta}{\eta}\left[1 - \frac{\Psi(z)}{\zeta}\right] \quad \textbf{(5.1)}$$

Where ε denotes the permittivity of the buffer solution, ε_0 denotes the permittivity of free space, E is the applied potential field strength, ζ is the zeta potential of the channel when in contact with a electrolytic solution of a given ionic strength, η is the viscosity of the buffer, and $\Psi(z)$ is the electrostatic potential distribution as defined by Garcia *et. al*. [78].

As shown in previous studies [78] the flux of particles within these nanofluidic devices can be described by taking the product of the local velocity by the particle concentration at that position. In order to calculate the concentration distribution of proteins suspended in our nanofluidic channel, we first assume that the proteins are rigid

and spherical with a radius R_p. By conservation of mass, and by assuming continuity, the concentration within a nanochannel can be described by Equation 5.2.

$$\frac{\partial C}{\partial t} + \nabla N = 0 \tag{5.2}$$

Where C is the protein concentration and N is the total flux of the proteins in solution. This concentration gradient accounts for the interaction between the nanochannel walls and the proteins due to the electrostatic repulsion caused by double-layer developed from both surfaces (DL), and the attraction forces caused by van der Waals forces (VDW). The total flux of these suspended proteins consists of two components (in the x-, and z-directions) as shown in Equation 5.3.

$$\begin{aligned} N_x &= u_p C - D_x \frac{\partial C}{\partial x} \\ N_z &= (v_s) C - D_z \frac{\partial C}{\partial z} \end{aligned} \tag{5.3}$$

Where u_p is the protein velocity, $D_{x,\,z}$ are the diffusion coefficients in x and z, and v_s is the total transverse protein velocity due to the surface forces ($v_s = v_{DL} + v_{VDW}$); v_{DL} and v_{VDW} are the particle velocities due to double-layer and van der Waals forces respectively.

To simplify the solution, the adsorption of the proteins to the surface of the walls is neglected. The adsorption effect is minimized in experimental efforts with the addition of surfactants to the buffer solution. Therefore the total flux in the *z*-direction at the wall surface is zero, and Equation 5.3 becomes Equation 5.4.

$$\frac{\partial C}{\partial z} = \left(\frac{v_s}{D_z}\right)C \tag{5.4}$$

In order to integrate with respect to *z* we must first define the integrating factor shown in Equation 5.5.

$$\beta(z) = e^{\int\left(-\frac{v_s}{D_z}\right)dz} \tag{5.5}$$

Thus, because it's a linear first order differential equation, we can say that: $\frac{d}{dz}\left[\beta(z)C(z)\right] = 0$, and the concentration distribution can be described by Equation 5.6.

$$C(z) = \alpha e^{\frac{-\int v_s dz}{D_z}} \tag{5.6}$$

Where α is an integration constant, and can be determined by boundary conditions.

The velocity due to surfaces forces, v_s, can be calculated by Stokes's law, in terms of the surfaces forces (F) as shown in Equation 5.7.

$$v_s(z,R_p) = \frac{F(z,R_p)}{6\pi\mu R_p} \tag{5.7}$$

In turn, the surfaces forces can be calculated by taking the differential of the interaction potential energy (ϕ) between the protein and the wall, shown in Equation 5.8.

$$F(z,R_p) = -\frac{\partial(\phi_{DL} + \phi_{VWD})}{\partial z} \tag{5.8}$$

This double-layer interaction energy has been explored previously [98,99] and modified for our system as described by Equation 5.9.

$$\phi_{DL} = \frac{Y_1 Y_2 Y_3}{1 + \left[1 - Y_5 Y_6\right]^{1/2}} \left(Y_4(z) + Y_4(d-z)\right) \tag{5.9}$$

With:

$$Y_1 = 32\varepsilon R_p\left(\frac{kT}{e}\right),\ Y_2 = \tanh\left(\frac{e\zeta}{4kT}\right),\ Y_3 = \tanh\left(\frac{e\zeta_p}{4kT}\right),\ Y_4(z) = \exp(-\kappa z),\ Y_5 = \frac{2R_p\kappa + 1}{\left(R_p\kappa + 1\right)^2},$$

$$Y_6 = \left[\tanh\left(\frac{e\zeta_p}{4kT}\right)\right]^2$$

where e is the elemental charge, κ is the Debye screening parameter ($\kappa = \sqrt{\frac{e^2(z_z^2 n_1 + z_2^2 n_2)}{\varepsilon\varepsilon_0 kT}}$), and z is the separation distance between the particle and the wall.

Equation 5.10 describes the potential energy due to van der Waals forces [100].

$$\phi_{VDW} = \frac{A}{6}\left[\ln\left(\frac{z+2R_p}{z}\right) - 2\left(\frac{R_p}{z}\right)\left(\frac{z+R_p}{z+2R_p}\right)\right] + \frac{A}{6}\left[\ln\left(\frac{(d-z)+2R_p}{(d-z)}\right) - 2\left(\frac{R_p}{(d-z)}\right)\left(\frac{(d-z)+R_p}{(d-z)+2R_p}\right)\right] \quad \textbf{(5.10)}$$

where A is the Hamaker constant, and is estimated here to be 1.1 x 10^{-21}. [101]

Now that we know the interaction potential energies, we can then substitute those terms into Equation 5.6 to get the concentration distribution in terms of the potentials. Noting that $\phi_{tot} = \phi_{DL} + \phi_{VDW}$, we can define the concentration distribution and concentration weighted particle velocity as shown in Equation 5.11.

$$C(z) = \alpha e^{\left(-\phi_{tot}/kT\right)}, \qquad u_p(z) = C(z)u(z) \tag{5.11}$$

Again, the average velocity of a protein molecule can be calculated by multiplying the local particle velocity by the protein concentration at that position. Neglecting the rotation of a protein molecule, the average velocity is defined in Equation 5.12.

$$\overline{u}_p = \frac{u(z)C(z)}{\frac{1}{d}\int_0^d C(z)dz} \tag{5.12}$$

5.3.1 Simplifications in the Theory

A simplified model has been created describing the use of hydrodynamic chromatography for separations of macromolecules in microfluidic channels. This model neglects both double-layer and van der Waals effects, and relies primarily on the exclusion of the larger molecules from the slower flow regions. Other studies have shown [102] that the approximation for the relative transport factor shown in Equation 5.13, is accurate for $R_p/b < 0.01$ and sufficiently accurate for $R_p/b < 0.1$. This indicates that the main mechanism behind the differences in residence time in open tubular HDC is the exclusion from the wall.

$$R_f = 1 + \frac{R_p}{b} - \frac{1}{2}\left(\frac{R_p}{b}\right)^2 \tag{5.13}$$

where, R_f is the relative transport factor, which can be defined as the ratio of the average rate of transport of the macromolecules in question divided by the average rate of the bulk fluid. [96] With this, we can estimate the average protein molecule velocity in terms of this relative transport factor, shown in Equation 5.14.

$$\overline{u}_p = \overline{u}_o R_f \tag{5.14}$$

Because this simplified model was developed for pressure driven flow, with a parabolic velocity distribution, it does not exhibit good of agreement with our experimentally observed data. It was included here because the calculation can be done quickly and gives a relative qualitative idea about the expected velocity of particles like proteins within nanochannels.

5.3.2 Plots

Since the majority of experimental efforts focused on using nanofluidic chips that had a channel width of ~100 nm, the results of the analytical model presented here focus on channels of that size. The simulation modeled a system with a 1/100 x dilution of standard Tris-Glycine gel electrophoresis buffer [78], that had two spherical, non-rotating analytes with radii 1.1 nm and 4.75 nm (representing the proteins trypsin inhibitor and R-Phycoerythrin respectively) suspended within it. In most studies the hydrodynamic radius of the protein is modeled at a percentage (85-90%) of the measured protein radius [103], however, we used the entire protein radius in our study to account for the increase in

particle size due to being encapsulated in a surfactant micelle. The change in concentration of the buffer system due to the introduction of charged analytes was neglected.

First we had to characterize the electrostatic potential within one nanochannel. The electrostatic potential distribution was calculated using a superposition of the electrical double layer that arises from each wall. [104] The resulting potential $\Psi(x)$ can be seen in Figure 49.

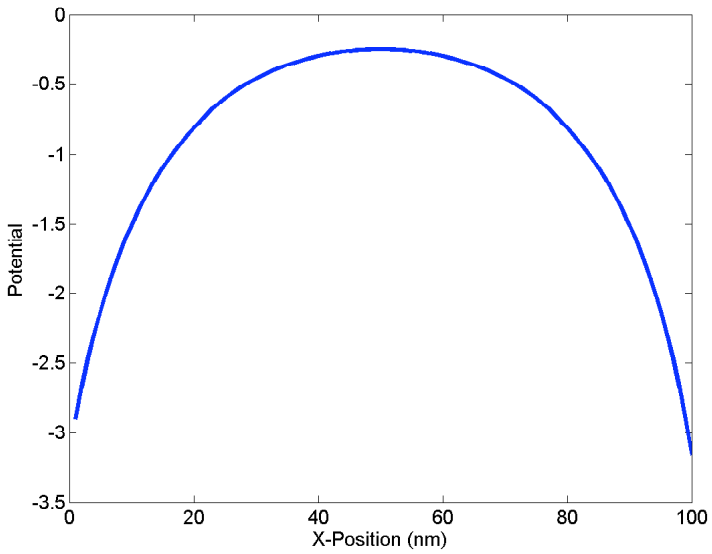

Figure 49: Electrostatic potential distribution within 100 nm wide channel.

The resulting potential energy field within the nanochannel was then calculated for each particle per Equation (7), shown in Figure 50. This accounts for the interaction

of the double layers that arise from the channel walls with the double layers that arise from the protein's surface.

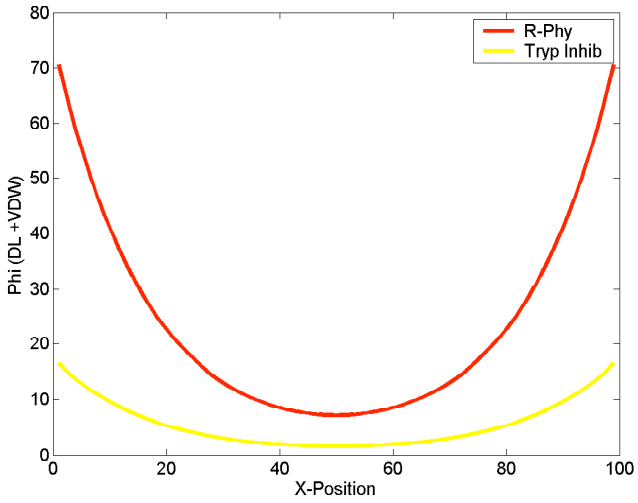

Figure 50: Total potential energy distribution within a nanochannel $\phi_{tot} = \phi_{DL} + \phi_{VDW}$

The model also accounts for van der Waals forces, which act as an attraction force and produce a particle velocity towards the channel walls, and slows the protein molecules net forward flux. The resulting velocity component due to van der Walls effects is shown in Figure 51. In a 100 nm wide channel, van der Waals forces do not significantly affect transport except in regions very near the channels walls. Here, the van der Waals effects decay over a much shorter length than the corresponding double layer effects. However as channel width decreases, it can be seen that van der Waals forces can become more significant in describing particle transport.

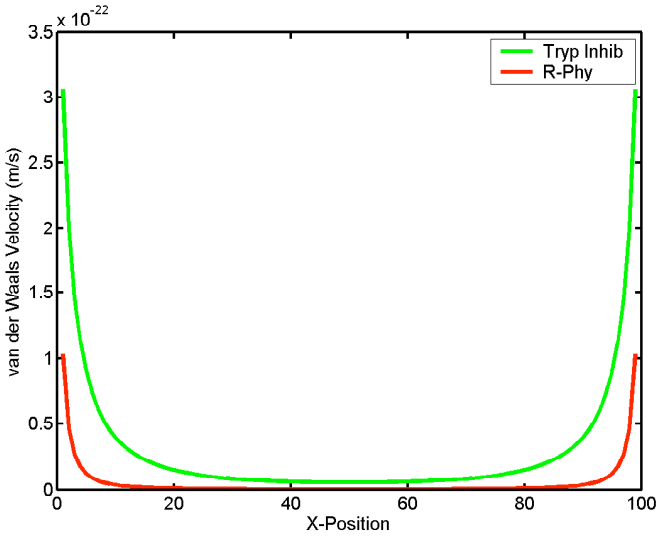

Figure 51: Velocity due to van der Waals forces showing this does not significantly effect protein velocity under the conditions and channel size in this simulation.

The resulting concentration profile along the width of a nanochannel was then calculated via Equation (11), and a normalized concentration profile was plotted as shown in Figure 52. This demonstrates the exclusion of the larger particles from the regions near the channel walls by a distance that is greater than the approximate radii of the particle. This increase in size of the exclusion region is attributed to double layer interactions.

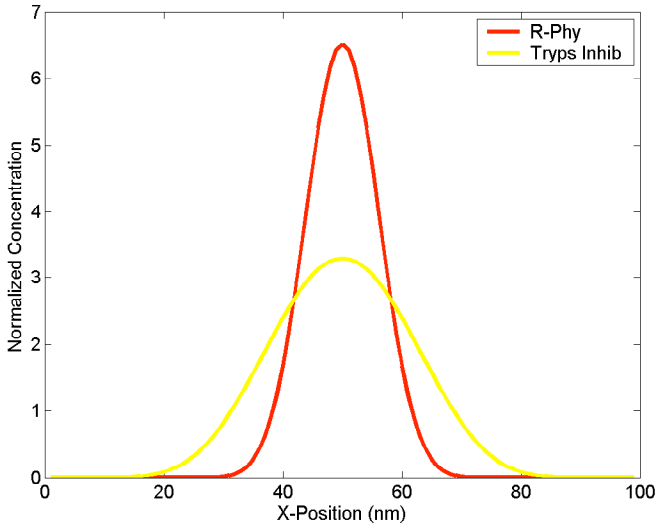

Figure 52: Normalized concentration profile of proteins along the width of a nanochannel.

The resulting electroosmotic velocity was then calculated by taking the product of the local particle concentration with the local bulk electroosmotic velocity. The resulting flux, along with the bulk electroosmotic flux, is shown in Figure 53. This demonstrates an overall increase in the particle velocity in a nanochannel due to the hydrodynamic chromatographic exclusion effects.

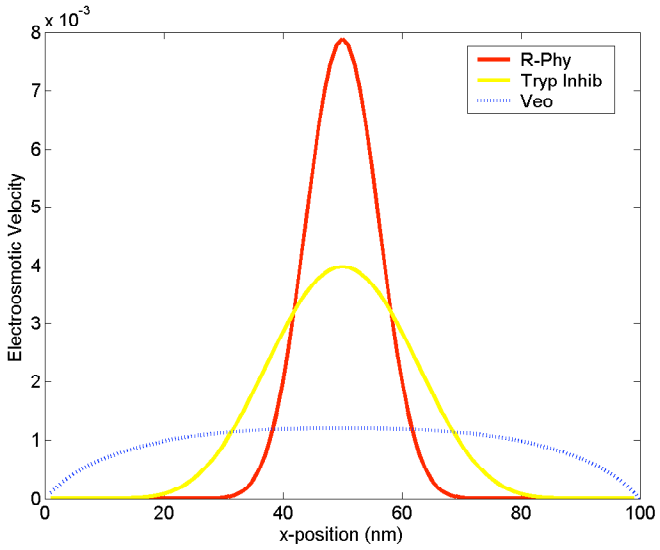

Figure 53: Concentration weighted velocity distribution of proteins in nanofluidic channel. The dotted line denotes the velocity profile of bulk buffer solution.

Simulations were run at various channel widths (analogous to different double layer lengths and different buffer ionic strengths). The results of simulations in narrower channels, 35 nm and 10 nm wide, are shown in Figure 54. This demonstrates that the overall electroosmotic velocities decrease as channel width decreases, and also demonstrates a breakdown in the model as the channel width approaches the size of the particle radius. This model holds for values of $d/R_p > 4$.

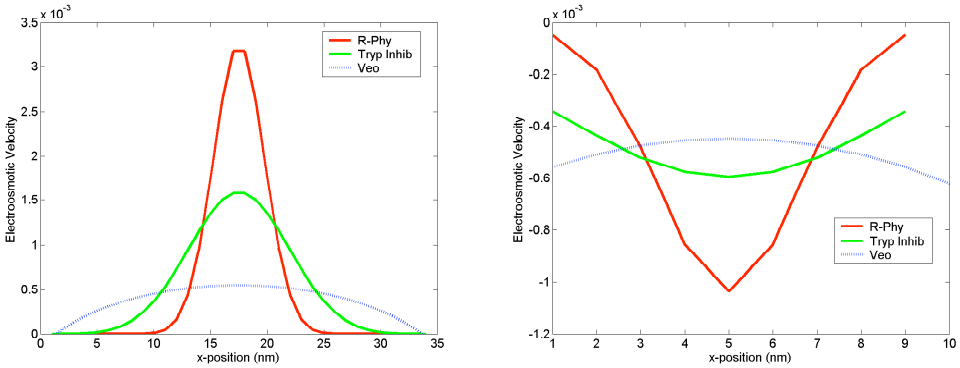

Figure 54: Velocity distributions in channels with widths of 35 nm (left) and 10 nm (right). The micrograph on the right demonstrates the model break down as the particle radius approaches the channel width.

The results of several electroosmotic velocity simulations run at various channel widths are shown in Figure 55. Experimentally derived velocities for systems with these proteins and channel widths of 35 and 100 nm are also plotted. The analytical model produces results that coincide within the calculated error of the experimentally measured velocities, which is indicative of the validity of the model. The calculated velocities of the two proteins studied here converge in channels that are approximately 450 nm wide. This coincides with the predicted cross over point between the nano- and micro- regimes that was previously found to be in ~400 nm wide channels for buffers with the same ionic strength as the one used here. [78]

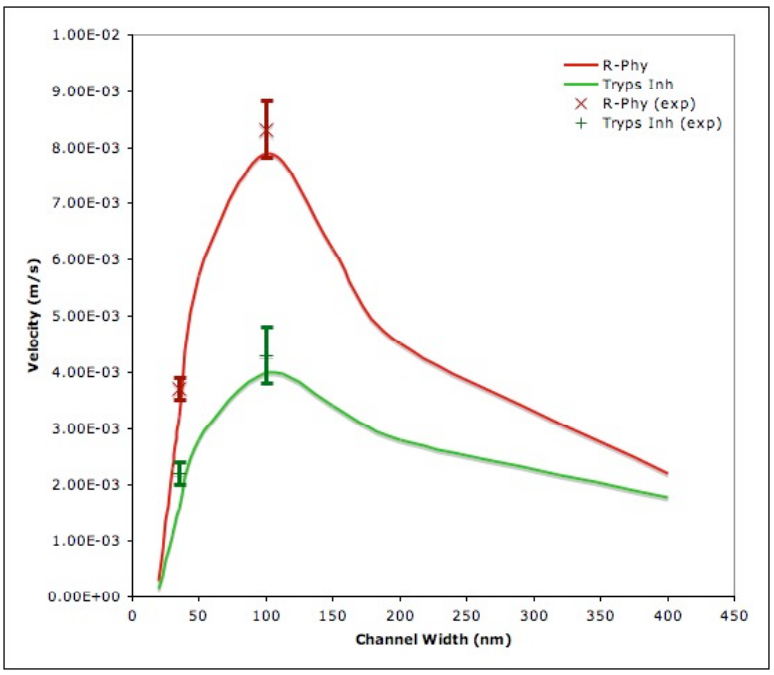

Figure 55: Experimental and theoretical protein velocities demonstrating good agreement with the separation model that factors in hydrodynamic chromatography like effects.

5.4 Protein Conclusions:

In conclusion, we have been able to demonstrate several mechanisms that are unique to nanofluidic systems that can be exploited to achieve separations of biomolecules, specifically proteins, on a chip-based device. In one mechanism, the interface between micro- and nanofluidic channels can be used to produce sieving like separations, in which the nanochannel region of the chip acts as a gate that only allows stable, less adsorptive, and smaller proteins to pass. Using this method for separations, results in a purified protein of interest, while leaving regions of concentrated proteins that

cannot pass through the nanochannel array in specific areas of the chip where they can be harvested for further study.

This effective nanofluidic gate can in turn be opened with the addition of surfactants to the buffer. Small quantities of the once blocked proteins can enter the nanochannel array when small, less than the CMC, amounts of surfactant are added, and can be fully allowed to enter the nanochannels when surfactant is added at or above the CMC. The addition of anionic surfactants, like SDS, allow for some blocked proteins to enter (and leave) the nanochannel area, providing a way to clear the channels, and transport mixtures of specific proteins through the nanochannel array without separating them. Separations were not observable with the addition of SDS because this surfactant increased the ionic strength of the running buffer, and decreased the double layer length, which is necessary for nanofluidic separations to occur.

Separations within the nanofluidic channels were observed when a nonionic surfactant, Tween 20 at its CMC, was added to the running buffer. This allowed protein-micelle conjugates to enter the nanochannel array without decreasing the double layer effects. Because these protein-micelle conjugates had similar valences, as demonstrated in microfluidic experiments, previous models could not explain the separations that were observed. A new hydrodynamic chromatography like model, based on the exclusion of larger molecules from the channel walls, was developed in this study. This model takes advantage of the non-plug-like electroosmotic velocity distribution that is unique to nanofluidic systems, to predict differential particle velocities do to their size differences.

This velocity difference can then be exploited as a nanofluidic sized based separation mechanism. A high level of agreement between the experimentally measured velocities and the predicted velocities demonstrates the validity of the model.

The work shown in this study provides the framework for future experimental and theoretical studies of biomolecular transport in nanofluidic devices. For the first time, experimental validation that demonstrates how proteins can be predictably transported within nanofluidic channels is shown here. Finally this study, in which simple protein mixtures can be separated in simple nanofluidic architectures, provides the groundwork for future studies in which more complex purification systems and separation devices can be developed.

Chapter 6: Conclusions/Recommendations:

The scaling down of fluidic systems to the nano regime has provided researchers with techniques to observe the fundamental properties of liquids and molecule interactions as well as granted access to new tools to perform fast and efficient separations. While much progress has been made recently, the study of nanofluidics, specifically in biomolecular separation systems, is still in the early stages of development. Work can still be done to improve the fabrication, layout, and channel geometry of these systems in order to best take advantage of the unique phenomena that occur in nanofluidic conduits that allow for separation. The use of semiconductor substrates as a platform for these nanochannels foreshadows the further exploration of microchip-like fluidic systems.

The use of field effect transistor like devices to control analyte flow within nanochannels has been studied, but methodologies must still be perfected in order to achieve fully controllable molecular transport and separations. Also, the use of parallel nanofluidic systems can be explored for the transport of information, since each molecule that is transported can represent complex data, leading to computational uses. Methods of improving the detection of the transported analytes within these channels must also be done to quantify separations of multi-analyte systems as well as take advantage of the size and portability of these schemes.

Furthermore, detection techniques can also be developed to increase the portability of these systems. Because of the small footprint and voltages needed to perform separations these systems are amenable to portable larger scale systems. However, one of the remaining major obstacles in increasing the portability of these devices is in the development of detection strategies. Currently the detection and characterization of the analytes in nanofluidic systems is performed with relatively large-scale laboratory equipment such as microscopes. If smaller, less energy consuming detection schemes are developed; these devices become more feasible for more versatile uses.

The theory of transport in nanochannels also needs further development. Particularly difficult problems include the motion of charged particles that have comparable sizes that the channels width, anisotropic and irregular shapes or non-uniform surface charge distribution. Experimental work needs to be done in the regime where continuum theory breaks down to validate existing models. This has become possible with the fabrication techniques explored in this dissertation.

Finally, the aspiration in this research is to integrate these nanofluidic devices into larger total analytical systems that can be used for chemical collection, separation, detection, and analysis. The chip based nanofluidic platform lends itself to integration with many common mass spectrometers in use today. Also the very nature of using chip-based platforms suggests that these systems can be computer controlled, high-throughput, automated separation devices.

Many exciting nanofluidic phenomena have already been harnessed, with much more progress to come.

References

Chapter 1: Introduction References:

[1] Kemery, P.J.; Steehler, J.K.; Bohn, P.W.; *Langmuir.* **1998**, 14, 2884-2889.

[2] Becker, H.; Lowack, K.; Manz, A. *J. Micromech. Microeng.* **1998**, 8, 24-28.

[3] Jacobson, S.C.; Alarie, J.P.; Ramsey, J.M. *Procedings of Micro Total Analysis Systems* **2002**

[4] Hibara, A.; Saito, T.; Kim, H.B.; Tokeshi, M.; Ooi, T.; Nakao, M.; Kitamori, T. *Anal. Chem.* **2002**, 74, 6170-6176.

[5] Kuo, T.C.; Cannon, D.M.; Chen, Y.; Tulock, J.J.; Shannon, M.A.; Sweedler, J.V.; Bohn, P.W. *Anal. Chem.* **2003**, 75, 1861-1867.

[6] Pennathur, S.; Santiago, J.G. *Anal.Chem.* **2005**, 77, 6782-6789.

[7] Karnik, R.; Fan, R.; Yue, M.; Li, D.; Yang, P.; Majumdar, A. *Nano Lett.* **2005**, 5, 943-948.

[8] Han, J.; Craighead, H.G. *Science*, **2000**, 288, 1026-1029.

[9] H. Cao, Z. Yu, J. Wang, J. O. Tegenfeldt, R. H. Austin, E. Chen, W. Wu, S. Y. Chou, *Appl. Phys. Lett.* 2002, *81*, 3058.

[10] Fu, J.; Mao, P.; Han, J. *Applied Physics Letters*, **2005**, 1, 352- 355.

[11] Vankrunkelsven, S.; Clicq, D.; Cabooter, D.; Malsche, W.D.; Gardeniers, J.G.E.; Desmet, G. *J. Chomatography A.* **2006**, 1102, 96-103.

[12] Karnik, R.; Castelino, K.; Majumdar, A. *Applied Physics Letters* **2006**, 88, 123114.

[13] Schoch, R.B.; Bertsch, A.; Renaud, P. *Nano Lett* **2006**, 6, 543-547.

[14] Yao, D.; Anex, D.S.; Caldwell, W.B.; Arnold, D.W.; Smith, K.B.; Schultz, P.G. *PNAS* **1999**, 96, 5372-5377

[15] Burns, M.A.; Johnson, B.N.; Brahmasandra, S.N.; Handique, . ;Webster, J.R.; Krishnan, M.; Sammarco, T.S.; Man, P.M.; Jones, D.; Heldsinger, D.; Mastrangelo, C,.H.; Burke, D.T. *Science* **1998**, 282, 484-487.

[16] Kim, S.M.; Burns, M.A.; Hasselbrink, E.F. *Anal. Chem.* **2006**, 78, 4779-4785.

[17] R. Qiao, and N.R. Aluru; *Simul. Microsystems*; v.28 (2002).

[18] A. Acrivos, B. Khusid, J. Koplik, G. Drazer; *Model. Simul. Microsystems*. v.66. (2002).

[19] B.B. Haab, R.A. Mathies; *Anal. Chem*. v.71, pp. 5137 (1999).

[20] J. Han, H.C. Craighead; *Anal. Chem*. v.74, pp. 394 (2002).

[21] H. Cao, Z. Yu, J. Wang, J.O. Tegenfeldt, R.H. Austin, E. Chen, W. Wu, S.Y. Chou; *Appl. Phys. Lett*. v.81, pp.174 (2002).

[22] H.G. Craighead; *Science*. v.290, pp. 1532 (2000).

[23] C.L. Rice, R. Whitehead; *J. Phys. Chem*. v.69, pp. 4017 (1965).

[24] X.J. Fan, N. Phan-Thien, N.T. Youg, X. Diao.; *Phys. Fluids* v.14, pp. 1146 (2002).

[25] C.K. Harnett, G.W. Coates, H.G. Craighead; *J. Vac. Sci. Technol. B*. v.19, pp. 2842 (2001).

[26] A. Hibara, T. Saito, H.B. Kim, M. Tokeshi, T. Ooi, M. Nakao, T. Kitamori; *Anal. Chem*. v.74, pp. 6170 (2002).

[27] H. Cao, J.O. Tegenfeldt, R.H. Austin, S.Y. Chou; *Appl. Phys. Lett*. v.81, pp. 3058 (2002).

[28] V. Studer, A. Pepin, Y. Chen; *Appl. Phys. Lett*. v.80, pp. 3614 (2002).

[29] S.Y. Chou, P.R. Krauss, P.J. Renstrom; *Appl. Phys. Lett*. v.67, pp. 3114 (1995).

[30] M. Colburn, A. Grot, B.J. Choi, M. Amistoso, T. Bailey, S.V, Sreenivasan, J.G. Ekerdt, C.G. Willson; *J. Vac. Sci. Technol. B*. v.19, pp. 2162 (2001).

[31] S. Zankovych, T. Hoffmann, J. Sekanp, J.U. Bruch, C.M.S. Torres; *Nanotechnology*. v.12, pp. 91 (2001).

[32] S.H. Zaidi, A.S. Chy, S.R.J. Brueck; *J. Appl. Phys.* v.80, pp. 6697 (1996)

[33] A.K. Raub, S.R.J. Brueck; *Proc. SPIE*. v.5040, pp. 667 (2003).

[34] S.C. Jacobson, J.M. Ramsey; in *High Performance Capillary Electrophoresis*, edited by M.G. Khaledi, Chemical Analysis Series Vol. 146 (Wiley, New York, 1998), pp. 613.

Chapter 2: Dye Separations References:

[35] Han, J.; Turner, S.W.; Craighead, H.G. *Phys. Rev. Lett.* 1999, **86**, 1394.

[36] Clicq, D.; Vervoort, N.; Vounckx, R.; Ottevaere, H.; Buijs, J.; Gooijer, C.; Ariese, F.; Baron, G.V.; Desmet, G. *Journal of Chromatography* 2002, **979**, 33.

[37] Jacobson, S.C.; Alarie, J.P.; Ramsey, J.M. *in Proceedings of Micro Total Analysis Systems* 2001, Dordrecht, The Netherlands, 2001 57-59.

[38] Karlsson, R.; Karlsson, M.; Karlsson, A.; Cans, A.S.; Bergenholtz, J.; Akerman, B.; Ewing, A.G.; Voinova, M.; Orwar, O., *Langmuir* 2002, **18**, 4186.

[39] Stein, D.; Kruithof, M.; Dekker, C. *Phys. Rev. Lett.* 2004, **93**, 035901.

[40] Cheng, J.T.; Giordano, N. *Physical Review E* 2002, **65**, 031206.

[41] Kemery, P.J.; Steehler, J.K.; Bohn, P.W., *Langmuir* 1998, **14**, 2884.

[42] Pu, Q.S.; Yun, J.S.; Temkin, H.; Liu, S.R. *Nano Lett.* 2004, **4**, 1099.

[43] Thompson, A.P. *J. Chem. Phys.* 2003, **119**, 7503.

[44] Travis, K.P.; Gubbins, K.E. *J. Chem. Phys*. 2000, **112**, 1984.

[45] Daiguji, H.; Yang, P.D.; Szeri, A.J.; Majumdar, A., *Nano Lett.* 2004, **4**, 137.

[46] Qiao, R.; Aluru, N.R.; *J. Chem. Phys*. 2003, **118**, 4692.

[47] Rice, C. L.; Whitehead, R. J. *Phys.Chem*. 1965, **69**, 4017.

[48] Hunter, R.J. *Zeta potential in colloid science: principles and applications*. Academic Press: London, 1981.

[49] O'Brien, M.J.; Bisong, P.; Ista, L.K.; Rabinovich, E.M.; Garcia, A.L.; Sibbett, S.S.; Lopez, G.P.; Brueck, S.J. *J. Vac. Sci. Technol. B* 2003, **21**, 2941.

[50] http://www.probes.com/

[51] Sinton, D.; Li, D.; *Colliods and Surfaces A: Physiochem. Eng. Aspects*. 2003, **222**, 273.

[52] Scales, P.J.; Greiser, F.; Healy, T.W.; White, L.R.; Chan D.Y.C *Langmuir* 1992, **8**, 965.

[53] Riley, D.J.; Carbonell, R.G. *Journal of Colliod and Interface Science* 1993, **158**, 259

[54] Russel, W.B.; Saville, D.A.; Schowalter, W.R. *Colloidal Dispersions* Cambridge University Press, 1989.

[55] Verwey, E.J.; Overbeek, J.T. *Theory and Stability of Lyophobic Colliods*. Elsevier: Amsterdam, 1948.

[56] Drazer, G. *Phys Rev Lett.* 2002, **89**, 244501.

[57] Kirby, B.J.; Hasselbrink, E.F. *Electrophoresis* 2004, **25**, 187.

[58] We also fit the data using a model with only adsorption driving the separation, using two fitting parameters representing the kinetic adsorption coefficients for each dye. This resulted in a negative adsorption coefficient for the negatively charged Alexa dye, meaning this dye exhibits negative

adsorption (i.e. repulsion which our model shows is likely due to Debye-layer effects).

[59] J.C.T. Eijkel, A. van den Berg. *Microfluidics and Nanofluidics*, v.1, No. 3, pp. 249 (2005)

Chapter 3: Pressure Separations References:

[60] C. L. Rice and R. Whitehead, *J. Phys.Chem*. v.69, pp. 4017 (1965).

[61] X.C. Xuan, and D.Q. Li. *Electrophoresis*. v.28, no. 4, pp. 627 (2007)

[62] X.C. Xuan. *Electrophoresis*. v.29, no. 18, pp. 3737 (2008).

[63] W.F. Zhang, and D.Q. Li. *Microfluidics and Nanofluidics*. v.3, no. 4, pp.417 (2007)

[64] A.L. Garcia *et al*., *LAB ON A CHIP*; v.5, no.11, p.1271 (2005)

[65] D.R. Petsev and G.P. Lopez, *Colliod and Interface Science*, v.294, no.2, p.492 (2006)

[66] A.M. Al-Ajloundi. *International Journal of Chemical Kinetics*. v. 37. p. 532 (2005)

[67] G.K. Batchelor. *An Introduction to Fluid Dynamics*, Cambridge University Press (1967),

[68] J. Pfitzner. *Anaesthesia* v.31. p. 273 (1976)

[69] D.N. Petsev. *Journal of Chemical Physics*. v. 123. p. 244907 (2005)

Chapter 4: Protein Separations References:

[70] K.S. Lilley, A. Razzaq, P. Dupree; *Current Opinion in Chemical Biology*. v. 6, no. 1, pp. 46 (2002).

[71] A. Daridon, M. Sequeria, G. Pennarun-Thomas, H. Dirac, J.P. Krog, *et. al*. *Sensors and Actuators B-Chemical.* v.76, no.1-3, pp. 235 (2001).

[72] A. Manz, Y. Miyahara, J. Miura, Y. Watanabe, H. Miyagi, *et. al*. *Sensors and Actuators B-Chemical*. v.1, no. 1-6, pp. 249 (1990).

[73] R.B.M. Shasfoort, S. Schautmann, L. Hendrikse, A. van den Berg. Science. v. 286, no. 5441, pp. 942 (1999).

[74] M.J. O'Brien, P. Bisong, L.K. Ista, E.M. Rabinovitch, A.L. Garcia, *et. al*. *Journal of Vacuum Science and Technology B*. v.21, no. 6, pp. 2941 (2003).

[75] LJ. Guo, X, Cheng, C.F. Chuo. *Nano Letters*. v. 4, no. 1, pp. 69 (2004).

[76] J. Han, H.G. Craighead, *Journal of Vacuum Science and Technology A-Vacuum Surfaces and Films*. v. 17, no. 4, pp. 2142 (1999).

[77] R. Karnik, R. Fan, M. Yue, D.Y. Li, P.D. Yang, *et. al*. *Nano Letters*. v. 5, no. 8, pp. 943 (2005).

[78] A.L. Garcia *et al*., *LAB ON A CHIP*; v. 5, no. 11, pp. 1271 (2005)

[79] S. Vankrunkelsven, D. Clicq, D. Cabooter, W. DeMalsche, *et. al*. *Journal of Chromatography A*. v. 1102, pp. 96 (2006).

[80] R. Karnik, K. Castelino, A. Majumdar. *Anal Chem*. v. 88, pp. 123114-1-3 (2006).

[81] R.B. Schoch, A. Bertsch, P. Renaud, *Nano Letters.* v. 6, pp. 543 (2006).

[82] M.A. Burns, B.N. Johnson, S.N. Brahmassandra, K. Handique, *et. al*. *Science*. v. 282, pp. 484 (1998).

[83] S. Yao, D.S. Anex, W.B. Caldwell, D.W. Arnold, *et. al*. *Proc. Natl. Acad. Sci. USA*. v. 96, pp. 5372 (1999).

[84] S.M. Kim, M.A. Burns, E.F. Hasselbrink. *Anal Chem*. v. 78, pp. 4779 (2006).

[85] Protein Data bank: http://www.rcsb.org/pdb/home/home.do

[86] E. Bayer,: "The Avidin-Biotin Complex", Dept. of Biological Chemistry, Weizmann Institute of Science, Israel

[87] K. Chunhee, and H. You-Lo. (2001). *Colloids and Surfaces A*. v. 187. pp. 385 (2001).

[88] P. Mukerjee, and K.J. Mysels. *NSRDS-NBS 36, US. Government Printing Office, Washington,.D.C.* (1971).

[89] F.O. Ayorinde, S.V. Gelan, J.H. Johnson, and L.W. Wan. *Rapid Communications in Mass Spectrometry*. v. 14. pp. 2116 (2000).

[90] J. Fu, R.B. Schoch, A.L. Stevens, S.R. Tannenbaum, and J. Han. *Nature Nanotechnology.* v. 2. pp. 121 (2007).

[91] J. Vidi, D. Su, M. Erceg, and D. Vucelic. *J. of Electroanalytcal Chem.* v. 452. pp. 151 (1998).

[92] R. Bashir, R. Gomez, A. Sarikaya, M.R. Ladisch, J. Sturgis, and J.P. Robinson. *Biotechnology and Bioengineering*. v. 73. pp. 324 (2001).

[93] X.C. Xuan. *Electrophoresis.* v. 1187, pp. 289 (2008).

[94] J. Han. *Introduction to Science and Technology.* pp. 575 (2004).

[95] E.A. DiMarzio and C.M. Guttman, *Macromolecules*, v. 3. pp. 131 (1970).

[96] H. Small, *J. Colloid Interface Sci.*, v. 48, pp. 147 (1974).

[97] Y.C. Lin and C.P. Jen. *Lab on a Chip.* v. 2. pp. 164 (2002).

[98] G.M. Bell, S. Levine and L.N. McCartney, *J. Colloid Interface Sci*. v. 33. pp. 335 (1970).

[99] H. Ohshima, T. W. Healy and L. R. White, *J. Colloid Interface Sci*. v. 90, pp. 17 (1982).

[100] H.C. Hamaker, *Physica*, v.4. pp. 1058 (1937).

[101] J. Visser. *Adv. Colloid. Interface Sci.* v. 3. pp. 331 (1972).

[102] D.C. Prieve and P.M. Hoysan. *Colloid Interface Sci*. v. 64. pp. 201(1978).

[103] M.T. Blom, E. Chmela, R.E. Oosterbroek, R. Tijssen, and A. van den Berg. *Anal. Chem.* v. 75. pp. 6761 (2003).

[104] D.N. Petsev. *Journal of Chem. Phys.* v. 123. pp. 244907 (2005).